

Stellar characterization with photometric colors from J-PLUS and 2MASS surveys.

J. F. Aguilar^{1,2}, P. Cruz³, E. Solano³, P. R. T. Coelho⁴, A. Ederoclitte^{5,6}, V. M. Placco⁷, P. Mas-Buitrago³, A. Alvarez-Candal⁸, A. J. Cenarro^{5,6}, D. Cristóbal-Hornillos⁵, C. Hernández-Monteagudo^{9,10}, C. López-Sanjuan^{5,6}, A. Marín-Franch^{5,6}, M. Moles⁵, J. Varela⁵, H. Vázquez Ramíó^{5,6}, J. Alcaniz¹¹, R. A. Dupke^{11,12}, L. Sodr e Jr.⁴, and R. E. Angulo^{13,14}

- ¹ PhD Programme in Astrophysics, Doctoral School, Universidad Aut noma de Madrid, Ciudad Universitaria de Cantoblanco, 28049 Madrid, Spain.
- ² Departamento de Matem ticas, Universidad Militar Nueva Granada, kil metro 2 v a Cajic  - Zipaquir , Colombia, c digo postal 110111. e-mail: john.aguilar@unimilitar.edu.co
- ³ Centro de Astrobiolog a (CAB), CSIC-INTA, Camino Bajo del Castillo s/n, E-28692, Villanueva de la Ca ada, Madrid, Spain.
- ⁴ Universidade de S o Paulo, Instituto de Astronomia, Geof sica e Ci ncias Atmosf ricas, 05508-090 S o Paulo, Brazil.
- ⁵ Centro de Estudios de F sica del Cosmos de Arag n (CEFCA), Plaza San Juan 1, 44001 Teruel, Spain.
- ⁶ Unidad Asociada CEFCA-IAA, CEFCA, Unidad Asociada al CSIC por el IAA y el IFCA, Plaza San Juan 1, 44001 Teruel, Spain.
- ⁷ NSF NOIRLab, Tucson, AZ 85719, USA.
- ⁸ Instituto de Astrof sica de Andaluc a – Consejo Superior de Investigaciones Cient ficas (IAA-CSIC), Glorieta de la Astronom a S/N,E-18008, Granada, Spain.
- ⁹ Instituto de Astrof sica de Canarias, La Laguna, 38205, Tenerife, Spain.
- ¹⁰ Departamento de Astrof sica, Universidad de La Laguna, 38206, Tenerife, Spain.
- ¹¹ Observat rio Nacional - MCTI (ON), Rua Gal. Jos  Crist v o, 20921-400 Rio de Janeiro, Brazil.
- ¹² University of Michigan, Department of Astronomy, 1085 South University Ave., Ann Arbor, MI 48109, USA.
- ¹³ Donostia International Physics Centre (DIPC), Paseo Manuel de Lardizabal 4, 20018 Donostia-San Sebasti n, Spain.
- ¹⁴ IKERBASQUE, Basque Foundation for Science, 48013, Bilbao, Spain.

Received XXX September 15, 1996; accepted March 16, 1997

ABSTRACT

Aims. We aim at deriving stellar atmospheric parameters based on the photometric data from the Javalambre Photometric Local Universe Survey (J-PLUS) in addition to near-infrared photometry from the Two Micron All-Sky Survey (2MASS).

Methods. Our method consists of a semi-supervised machine learning approach based on the k-means method combined with a modified k-nearest neighbors algorithm. This method compares the observed photometry to a set of reference data to estimate the stellar effective temperature (T_{eff}), surface gravity ($\log g$), and metallicity ($[\text{Fe}/\text{H}]$) of stars from J-PLUS Data Release 3 (DR3). For that, a set of 105 colors was constructed using extinction-corrected photometric data from J-PLUS DR3 and 2MASS. The reference dataset used was composed by the MESA Isochrones & Stellar Tracks (MIST) models, the Large sky Area Multi-Object fiber Spectroscopic Telescope (LAMOST), and the Apache Point Observatory Galactic Evolution Experiment (APOGEE) surveys.

Results. We estimated T_{eff} , $\log g$, and $[\text{Fe}/\text{H}]$, for approximately 5.6 million stars from J-PLUS DR3, along with their errors. Our results were in agreement with spectroscopic estimates from LAMOST and APOGEE. We also applied a dimension reduction method, seeking greater efficiency by reducing the computation time and minimizing the needed information for calculating the stellar parameters, resulting in a subset of 11 colors. From this approach, stellar parameters were obtained for approximately six million stars, increasing the number of studied objects. The obtained results were of the same order, despite having slightly higher uncertainties compared to those obtained with 105 colors.

Conclusions. Our results demonstrated the potential of using a method built from machine learning algorithms that do not require prior training. Additionally, it was shown that the proposed method allowed estimating reliable atmospheric parameters even when the available photometry did not fulfill all photometric quality criteria. As part of our method, we defined a neighborhood parameter, which assesses the reliability of our estimations and indicates that objects with smaller neighborhoods values have lower uncertainties.

Key words. methods:data analysis – stars: fundamental parameters –surveys –techniques:photometric

1. Introduction

The currently available information from large astronomical databases brought new possibilities for the study of stellar properties and evolution. For instance, photometric surveys in the optical and near-infrared, such as the Sloan Digital Sky Survey (SDSS; York et al. 2000), the *Gaia* mission (*Gaia*; *Gaia* Collaboration et al. 2016), the Two-micron All Sky Sur-

vey (2MASS; Skrutskie et al. 2006), The Southern Photometric Local Universe Survey (S-PLUS; Mendes de Oliveira et al. 2019) and the Javalambre Photometric Local Universe Survey (J-PLUS; Cenarro et al. 2019), have generated extensive, accessible databases that enable statistical analyses and the application of machine learning (ML) methods. ML techniques have made it possible to study specific characteristics along with a large number of associated variables. In particular, un-

supervised and clustering techniques have been useful tools for automated classification. For instance, the k-means clustering method (Jain & Dubes 1988) has been shown to be a robust approach, and it is regularly used in data mining and artificial intelligence to recognize patterns and trends (e.g., Everitt 1995; Bishop & Nasrabadi 2007). Among different applications in astronomy, such techniques are frequently applied to classify both galaxies and stars.

Based on automated classification techniques, Sánchez Almeida & Allende Prieto (2013) applied unsupervised k-means clustering to a massive set of stellar spectral data from SDSS, classifying stellar spectra into groups defined solely by the intrinsic properties of the data, distinguishing between dwarf and giant stars at similar temperatures. Using the same ML technique, Morales-Luis et al. (2011) systematically searched for extremely metal-poor galaxies in SDSS DR7 (Abazajian et al. 2009) using spectral shape analysis around $H\alpha$, and identified galaxies with metallicities ten times lower than solar. Other works used similar clustering techniques and spectroscopic information to distinguish among galaxies and quasars (Bailer-Jones 2008) or young stellar clusters with spectral information (Hojnacki et al. 2007).

There are various methodologies used to estimate stellar parameters, from classical spectroscopic approaches, recently combined with machine learning techniques, to methods based purely on photometry. Sprague et al. (2022a) have derived effective temperatures (T_{eff}), surface gravities ($\log g$), and metallicities ($[\text{Fe}/\text{H}]$) using a convolutional neural network (CNN)-based method. For that, they used high-resolution spectra obtained from the Apache Point Observatory Galactic Evolution Experiment project (APOGEE; Zasowski et al. 2013) from the 17th data release (DR17; Abdurro'uf et al. 2022). The parameter determination was performed by comparing observed spectra with a grid of synthetic spectra, such as those from Kurucz (1979, 1993), Coelho et al. (2005), and Husser et al. (2013).

Concerning photometry, Whitten et al. (2019) developed a neural network-based pipeline Stellar Photometric Index Network Explorer (SPHINX), for the photometric estimation of stellar atmospheric parameters using data from the J-PLUS DR1 (Cenarro et al. 2019). The SPHINX system was trained with synthetic photometry derived from medium-resolution SDSS spectra and calibrated with the J-PLUS photometric system. Their method was applied to the globular cluster M15, retrieving metal-poor stars with $[\text{Fe}/\text{H}] < -2.0$ dex. Yang et al. (2022) used data from J-PLUS DR1, and from *Gaia* DR2 (Gaia Collaboration et al. 2018), and spectroscopic labels from the Large sky Area Multi-Object fiber Spectroscopic Telescope (LAMOST; Deng et al. 2012) to obtain atmospheric parameters for a set of about two million stars. They designed and trained a set of cost-sensitive neural networks to estimate T_{eff} , $\log g$, and $[\text{Fe}/\text{H}]$, α -elements ($[\alpha/\text{Fe}]$), and four other elemental abundances.

Subsequent analyses of J-PLUS Data Release 2 (DR2; López-Sanjuan et al. 2021) involved the development and application of Stellar Parameters Estimation based on Ensemble Methods (SPEEM pipeline by Galarza et al. 2022, which utilized machine learning models trained to estimate stellar atmospheric parameters. This approach enabled the identification of 177 very metal-poor star candidates. Quispe-Huaynasi et al. 2023 used J-PLUS DR2, combined with *Gaia* DR3 astrometry, to characterize 28 high-velocity stars. They used a convolutional neural network (CNN) and a χ^2 fitting of spectral energy distributions (SEDs) using the Virtual Observatory SED Analyzer (VOSA;

Bayo et al. 2008) to derive stellar parameters and investigate the kinematics, dynamics, and possible origins of these stars.

Wang et al. (2022) developed a similar work, where they used a support vector regression (SVR) algorithm to derive T_{eff} , $\log g$, and $[\text{Fe}/\text{H}]$ for around 2.5 million stars in J-PLUS DR1. Later, Huang et al. (2024) studied the same stellar parameters for around five million stars, based on colors from J-PLUS DR3 (López-Sanjuan et al. 2024) and *Gaia* EDR3 (Gaia Collaboration et al. 2021), using methods like Kernel Principal Component Analysis (KPCA) and Bayesian methods.

The method adopted by previous works requires extensive training and often leads to some spurious solutions due to extrapolations. In order to avoid that, we employed a semi-supervised ML method chosen to avoid extreme outliers, that is based on the k-means technique, combined with a modified k-nearest neighbors (KNN) regression method (Cover & Hart 1967), to determine stellar atmospheric parameters. We estimated T_{eff} , $\log g$, and $[\text{Fe}/\text{H}]$ using photometry from J-PLUS DR3, combined with the near-infrared counterpart from 2MASS. An additional aim was to assess the effect that photometric quality may have on the inferred parameters.

This work is presented as follows. In Sect. 2, we present the models and observational data used. The implementation of the proposed method is described in Sect. 3. In Sect 4, we present our results, and in Sect. 5 our discussion. Our conclusions are presented in Sect. 6.

2. Data

2.1. Photometric data from J-PLUS DR3

The J-PLUS survey, operating in the Javalambre Astrophysical Observatory (OAJ), observes the sky with a collection of 12 broad-, intermediate-, and narrow-band optical filters – u , $J0378$, $J0395$, $J0410$, $J0430$, g , $J0515$, r , $J0660$, i , $J0861$ and z – covering important spectral features such as, for instance, the Balmer break region, $H\delta$, Ca II H and K lines, the G band, and the Ca II triplet (Cenarro et al. 2019). In its third data release (J-PLUS DR3; López-Sanjuan et al. 2024), it has over 47 million objects observed from a large area of around 3284^1 deg² of the sky.

J-PLUS DR3 provides criteria to identify objects with a high probability of being stars. We adopted the SExtractor's CLASS_STAR and the Bayesian star-galaxy separation prob_class_star, both available in the J-PLUS catalog, as described in López-Sanjuan et al. (2019). Both quantities take values from 0 to 1, with 0 corresponding to a galaxy and 1 to a star. We selected objects with values greater than or equal to 0.85 in both cases. By choosing this number, we minimized the differences between the two parameters mentioned above in objects assigned as stars. After we applied both class criteria, it resulted in a selection of 7 400 214 objects.

We also used photometric data in J , H , and K_s bands from the 2MASS survey (Skrutskie et al. 2006). We cross-matched the selected objects to 2MASS using the Virtual Observatory tool TOPCAT² (Taylor 2005, 2011). For this cross-matching, we used a 5 arcsec radius, taking this as the maximum difference between the coordinates in both catalogs. We kept only those objects that have magnitudes available for the complete set of 15 filters (12

¹ After masking, the area is ~ 2881 deg² (see López-Sanjuan et al. 2024, for details).

² TOPCAT is an interactive Tool for OPERations on Catalogues And Tables, available at <https://www.star.bris.ac.uk/~mbt/topcat/>. This and all further data arrangements were performed using TOPCAT.

from J-PLUS and 3 from 2MASS), which resulted in a total of 6 246 451 stars in our final sample.

The extinction map from [Schlegel et al. \(1998\)](#) is available in J-PLUS DR3 catalogs³ and it was adopted for reddening corrections in J-PLUS magnitudes. This map provides the line-of-sight $E(B - V)$ color excess integrated to infinity, which is nonetheless reasonably reliable for J-PLUS DR3, as the stellar sample predominantly lies at high Galactic latitudes. The 2MASS magnitudes were also corrected from interstellar extinction using the same extinction maps, where the $E(B - V)$ color excess was retrieved⁴ and the extinction in each band was computed according to the relation $A_\lambda = R_\lambda \times E(B - V)$, with R_λ values from [Yuan et al. \(2013\)](#).

One of the purposes of this study is to assess the effect that quality of the photometric data has on the inferred parameters, that is, if the method gives good approximations to the derived stellar parameters even if the quality of the photometry is somewhat compromised. For that, we divided our sample into two subsets. The high quality photometry (HQP) subset contains those objects whose photometry has specific quality flags depending on the survey. The "AAA"⁵ flag is associated with a good quality of the photometry of the three 2MASS filters; as well as FLAG and MASK_FLAG with a value of 0⁶ for each one of the 12 J-PLUS filters. The objects in the HQP subset must be sufficiently bright to minimize the impact of noise and instrumental uncertainties, which is why we required $r \leq 22$ mag. Moreover, all objects must have magnitude errors less than or equal to 5% in all 15 photometric bands, resulting in a subset of 1 922 570 stars. The remaining objects, those that do not meet one or more of the quality criteria mentioned above, compose the somewhat compromised photometry (SCP) subset, with 4 323 881 stars.

2.2. Reference data

We needed a reference sample with known T_{eff} , $\log g$, and $[\text{Fe}/\text{H}]$ values, and magnitudes available in all 15 bands to infer the stellar atmospheric parameters of the stars in our sample, as further described in Sect. 3. We gathered two different subsets: from spectroscopy and from stellar models.

The LAMOST survey ([Deng et al. 2012](#)) is conducted using a 4-meter quasi-meridian reflecting Schmidt telescope with 4000 fibers distributed over a field of view with 5 deg diameter ([Cui et al. 2012](#)). The stellar parameters available in LAMOST DR9⁷ ([Bai et al. 2021](#)) were estimated from low-resolution ($R \sim 2000$) SDSS-like optical spectra using the LAMOST Stellar Parameter Pipeline (LASPM; [Luo et al. 2015](#)).

We cross-matched our complete sample with LAMOST DR9, considering a 5 arcsec search radius, to obtain the needed spectroscopic labels, that is T_{eff} , $\log g$, and $[\text{Fe}/\text{H}]$ values derived from spectroscopy, to be associated to the magnitudes in all 15 bands (J-PLUS and 2MASS). It is worth emphasizing that the spectra were not used in our method. We then selected those ob-

jects that had LAMOST spectra with signal-to-noise ratio (SNR) greater than 10 and errors in their LAMOST stellar parameters of less than 5%, to ensure a great accuracy in the derived parameters, resulting in a total of 217 292 objects. A pseudo-random sample was defined in order to reduce the calculation time but keeping a sufficient number of objects that represented the different stellar parameter values available in LAMOST, composing a subset with 10 787 objects. Its coverage in stellar parameters is shown in Table 1.

Similarly, we performed a cross-match with APOGEE DR17 ([Sprague et al. 2022a](#)), which was conducted using two spectrographs mounted at two 2.5-meter telescopes – one at the Apache Point Observatory (APO), and one at the Las Campanas Observatory (LCO; [Bowen & Vaughan 1973](#); [Gunn et al. 2006](#)), with the ability to observe up to 300 sources in the H band (1.51–1.7 μm), with a resolution of $R \sim 22,500$, a field of view of 3° diameter in APO and 2° diameter in LCO ([Wilson et al. 2010, 2019](#)). We selected those objects with an error in stellar parameters of less than 5%, resulting in a total of 17 904⁸ objects. As done for LAMOST, a subset of 4 768 objects was selected through a pseudo-random sampling process, ensuring that the color distribution of the subset reproduces the one from the cross-matched sample. This representative subset was also used as reference data, as also shown in Table 1.

The APOGEE dataset was incorporated as reference data to cover ranges of atmospheric parameters that were not covered by the LAMOST reference data. It is worth emphasizing that in both cases the observed spectra were not used, only the derived stellar parameters were adopted as spectroscopic labels. The remaining LAMOST and APOGEE objects were considered as validation data, as explained in Sect. 2.3.

Stellar models were adopted to expand the parameter's range covered by our reference sample. Synthetic photometric data and the associated stellar parameters were obtained from the MESA Isochrones and Stellar Tracks⁹ project (MIST; [Dotter 2016](#); [Choi et al. 2016](#)), which is built on the Modules for Experiments in Stellar Astrophysics (MESA; [Paxton et al. 2011, 2013, 2015](#)) software. From these models the stellar parameters – T_{eff} , $\log g$, metal abundance (Z) – predicted by MESA are extracted and projected into the observational plane using synthetic photometry. The photometry is generated via bolometric correction tables computed from the C3K grid ([Choi et al. 2016](#)), which is based on the ATLAS12/SYNTH model atmospheres ([Kurucz 1970, 1993](#)). Although MESA provides the atmospheric parameters and evolutionary structure, the magnitudes in filters such as J-PLUS and 2MASS are derived from Kurucz-based color-temperature relations and synthetic spectra, meaning that the final results are based on Kurucz predictions processed using MESA outputs. By integrating both components, the MIST Packaged Model Grids¹⁰ gives the photometry and the stellar parameters: synthetic photometry in J-PLUS and 2MASS, together with the corresponding values of T_{eff} , $\log g$ and Z , for stars with metallicities ranging from $[\text{Fe}/\text{H}] \approx -4.0$ to $+0.5$ dex.

The J-PLUS filter set is not available in the MIST database among the available integrated synthetic photometry, therefore, we extracted those generated for S-PLUS as it has a filter system which is almost identical¹¹ to the one from J-PLUS. Finally, our

³ Available at [jplus.MWExtinction](#) table within the J-PLUS database.

⁴ The color excess was obtained using the SFDQuery class from the dustmaps Python package ([Green 2018](#)), which provides access to the extinction values by [Schlegel et al. \(1998\)](#).

⁵ Photometric quality flag "A" in a 2MASS band indicates that the corresponding magnitude measurement has a signal-to-noise ratio greater than 10 and a measurement uncertainty less than ~ 0.109 mag.

⁶ Objects with this value have no reported photometric extraction or image masking problems, indicating clean detections without saturation, decay complications, proximity to bright stars or edges, and are not affected by known masked artifacts in the image data.

⁷ Available at <http://www.lamost.org/dr9/v1.1/>.

⁸ These data are available at [Sprague et al. \(2022b\)](#).

⁹ Available at <https://waps.cfa.harvard.edu/MIST/>.

¹⁰ https://waps.cfa.harvard.edu/MIST/model_grids.html

¹¹ The S-PLUS filter system from the T80-South telescope and its large-format camera are also a duplicate of the system installed at T80/JAST telescope used in J-PLUS ([Mendes de Oliveira et al. 2019](#)).

Table 1. Range of stellar parameters covered by the different datasets considered.

Source	N	T_{eff} (K)		$\log g$ (dex)		[Fe/H] (dex)	
		Min	Max	Min	Max	Min	Max
<i>Reference data</i>							
LAMOST	10 787	3744	11720	0.932	4.900	-2.441	0.059
APOGEE	4 768	3186	6305	0.652	5.067	-1.945	0.324
MIST	5 510	2212	168845	-1.093	7.972	-4.000	0.500
<i>Validation data</i>							
LAMOST	206 505	3750	13422	0.719	4.900	-2.470	0.602
APOGEE	13 136	3186	10568	0.2037	5.151	-1.945	0.426
<i>Comparison data</i>							
Wang et al. (2022)	1 079 802	3578	8527	1.309	5.653	-2.552	-0.001
Huang et al. (2024)	2 385 202	2537	7700	1.002	5.099	-5.018	0

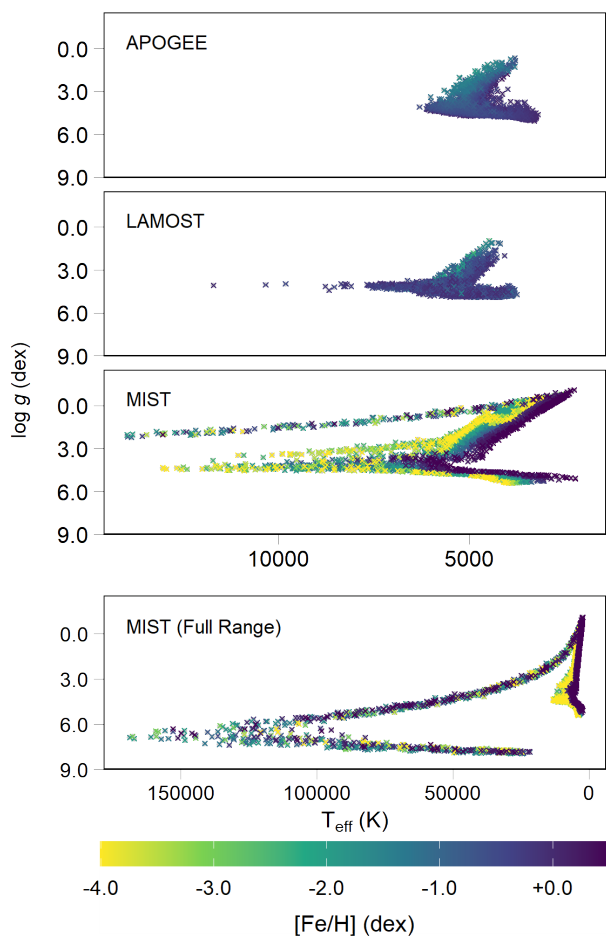


Fig. 1. Kiel diagrams for the reference dataset, including LAMOST, APOGEE, and MIST (2 times), in order from top to bottom. The upper three panels display observed data from LAMOST and APOGEE, and theoretical models from MIST, limited to T_{eff} between 2000 and 14000 K. The bottom panel shows the full temperature range of the MIST models, from 2212 to 168845 K.

synthetic reference subset contains 5 510 stellar models covering the loci of isochrones with $9 \leq \log(\text{age}) \leq 10.1$ and $v/v_{\text{crit}}=0.0$. This range was chosen to avoid very young phases (< 1 Gyr), which include pre-main sequence stars. The parameters coverage is also shown in Table 1.

Fig. 1 shows the Kiel diagram, illustrating that the reference sample contains a broad range of stellar parameters. Although

early-type or extremely metal-poor stars are the minority of objects expected in J-PLUS DR3, LAMOST or APOGEE, they are represented in the MIST models adopted to allow a wider diversity of parameters and their corresponding photometry in the studied 15 bands. MIST models are shown twice in Fig. 1 to highlight the stellar parameter ranges similar to those obtained from spectroscopy and also to show the complete range covered by our reference dataset.

2.3. Validation and comparison data

We defined a sample of stars that have their stellar parameters estimated from different methodologies and that were not considered as reference to assess the reliability of our results. They were divided into two groups: the validation set, with parameters estimated from spectroscopy, and the comparison set, with values estimated from photometric data and ML techniques.

We selected 206 505 objects from LAMOST DR9 as validation set, those that were not included in the reference dataset (see Sect. 2.2). Also, we added the remaining set of 13 136 objects from APOGEE DR17. The stellar parameters coverage for the validation dataset (for both samples, separately) is presented in Table 1.

Previous works have applied ML techniques to infer stellar parameters from J-PLUS data. We selected two of them to compare our results with, which compose our comparison sample. They are briefly summarized below.

Wang et al. (2022) estimated the same three stellar parameters for ~ 2.5 million stars in J-PLUS DR1 using a support vector regression (SVR) algorithm. The information used in training the data was the 12-band photometry from J-PLUS DR1, cross-matched with spectrum-based catalogs from LAMOST (LAMOST DR7; Luo et al. 2022) – low resolution spectra (LRS) and medium resolution spectra (MRS)¹² – from APOGEE (APOGEE DR16; Jönsson et al. 2020; Ahumada et al. 2020), and from the Sloan Extension for Galactic Understanding and Exploration (SEGUE; Yanny et al. 2009), specifically the SEGUE Stellar Parameter Pipeline (SSPP; Lee et al. 2008a,b). They built a catalog with 2 493 424 stars, where the estimated root mean square errors for T_{eff} , $\log g$, and [Fe/H] are 160 K, 0.35 dex, and 0.25 dex, respectively. We performed a cross-match between their catalog and our sample, excluding those that presented a quality flag¹³ or estimated errors over 5% in the

¹² <http://dr7.lamost.org/catalogue>

¹³ Wang et al. (2022) reported in their catalog, with an asterisk, some objects with less reliable stellar parameters.

derived parameters, finding 1 079 802 objects in common. These objects were used as a comparison set, as shown in Table 1.

Huang et al. (2024) adopted the Kernel Principal Component Analysis (KPCA) and Bayesian methods to derive stellar parameters and elemental-abundance ratios for around five million stars (mostly dwarfs) based on stellar colors from J-PLUS DR3 and *Gaia* EDR3. To build their model, they resorted to a large spectroscopic training set, which included catalogs such as SEGUE, LAMOST DR9, APOGEE DR17, and the GALactic Archaeology with HERMES (GALAH DR3; Buder et al. 2021) surveys. These objects were filtered, selecting only those with 5% error on the stellar parameters or a reliability flag equal to zero¹⁴. The 2 385 202 objects in common to our sample were also taken as part of our comparison set (see Table 1).

3. Methodology

Just as objects with similar spectroscopic profiles have similar T_{eff} , $\log g$, and $[\text{Fe}/\text{H}]$ values, it is to be expected that the behavior of stellar photometric colors will also be similar. Validating this idea implies thinking that objects with this information, which is represented here by the 105 colors under study, should be also similar to each other, and therefore, when represented in a \mathbb{R}^{105} space, should be grouped together. Considering that photometric observations have their associated errors and that they may have limitations in the inference of stellar parameters, we defined the concept of neighborhoods as regions in the \mathbb{R}^{105} space where objects with similar colors, i.e. stellar parameters, would be gathered. These neighborhoods may have different boundaries for different type of stars.

We adopted a modified version of the procedure described in Garrido et al. (2019); Cruz et al. (2022), based on the k-means algorithm (Jain & Dubes 1988), to derive the stellar parameters of millions of stars in J-PLUS DR3. The k-means algorithm, an unsupervised method, is combined with a modified version of the k-nearest neighbors (KNN) regression method (KNN; Cover & Hart 1967), a supervised approach, where the k neighbors that are contained within a given radius are taken instead of a typical constant number of neighbors. The method was implemented in a set of 105 colors, generated from the combination of the 12 J-PLUS bands (u , $J0378$, $J0395$, $J0410$, $J0430$, g , $J0515$, r , $J0660$, i , $J0861$, z), with those from 2MASS (J , H , K_s). The method was developed using the R software (R Core Team 2018), which consists of five steps as described in detail below.

Considering colors and stellar parameters from the reference data set (Sect. 2.2), we defined the number of clusters with similar characteristics that should be formed (step 1). To determine the optimal number of clusters, we applied the Hartigan test (Hartigan 1975), which is iterated 50 times to see a trend¹⁵ in the results and derive the optimum number of clusters. By analyzing the distribution of Hartigan statistics over multiple iterations, we ensured the stability of the clustering solution. The results consistently indicated a tendency to form 19 clusters, as determined from the median value of the Hartigan test across the 50 runs.

Once established the number of groups, the k-means method was implemented as follows. Taking again the reference sample as input data, we distributed them into 19 clusters and we defined the clusters centroids (step 2). This distribution is presented in Table A.1, showing that both synthetic (from MIST) and ob-

servational (from LAMOST and APOGEE) data that share the same cluster have similar characteristics in some of their stellar parameters. The observational data was found in four clusters only (2, 7, 11, and 17), where the remaining were populated by synthetic data only, given their stellar parameters.

In the second step, we also estimated pseudo-radii¹⁶ to describe neighborhood of objects with similar colors, and therefore stellar parameters, inside every proposed cluster.

Pseudo-radii (hereafter radii) are defined from the calculated distance (in \mathbb{R}^{105}) of each reference object to the centroid of its cluster. It is worth emphasizing that these distances generated a non-normal distribution, leading to radii that can take different values. Given this heterogeneity, we defined 10 radii regions based on statistical measures for each cluster, corresponding to the minimum, the 5th, the 25th, the 75th, the 95th, and the 99th percentiles, the mean, the median, the mode, and the maximum values¹⁷. A number from 1 to 10 (hereafter neighborhood) was associated to every region, with 1 being assigned to the smallest radius and 10 to the largest one.

Having defined the clusters and their centroids, we implemented the k-means algorithm for the second time to include our objects of interest (step 3). For that, we calculated the euclidean distance of each object in our target sample (Sect. 2.1) in the \mathbb{R}^{105} space to each one of the 19 centroids defined in step 2. The targets were considered as part of the clusters with the closest centroid.

We then searched for the nearest reference data within each cluster to estimate the stellar parameters of the objects in the target sample (step 4). They were identified based on the minimum neighborhood radius (from 1 to 10, among those mentioned earlier) that includes reference data on the assigned cluster. That is done as follows: first, we assume the radius assigned to neighborhood 1, centered on the objects position. If there are no reference data within the defined radius, we increase the region to neighborhood 2. This continues until the assigned neighborhood contains reference data. For the case where there is no reference data within all neighborhoods, the stellar parameter estimation is not performed, that is, we do not compute the parameters for that object.

Finally, the three stellar parameters (T_{eff} , $\log g$, $[\text{Fe}/\text{H}]$) were obtained for each target using a modified KNN method (step 5), which is based on the mean values considering the neighboring reference data, that is, those within the defined radius. The associated standard deviations were taken as the corresponding errors for the estimated parameters.

4. Results

Our method was applied to more than six million objects in our sample (Sect. 2.1). Among them, around 3% had previously been characterized spectroscopically by LAMOST and APOGEE. In Sect. 4.1, we describe the overall characteristics of our full dataset, while in Sect. 4.2, we compare our estimates to those surveys to assess the reliability of our results.

4.1. Overview of results with all colors

By implementing our method, we inferred the three stellar atmospheric parameters for 5 648 486 out of the 6 246 451 J-PLUS

¹⁴ Huang et al. (2024) also adopted a quality flag to define the reliability of the estimated values, with zero being the most reliable.

¹⁵ The differences in each of the iterations is due to the fact that the centroids are taken randomly.

¹⁶ They are called pseudo-radii because they may non-spherical shapes in the \mathbb{R}^{105} space.

¹⁷ The order of these values varies per cluster due to the heterogeneity of the distances described above.

Table 2. Summary of our sample using 105 colors, according to their spectral types. N is the number of objects in each class.

T_{eff} range (K)	Spectral type	N
10401–33300	B	1 299
7401–10400	A	10 568
6181–7400	F	256 115
5326–6180	G	2 368 356
3891–5325	K	2 471 419
2310–3890	M	540 729

DR3 objects with available photometry in all 15 bands (J-PLUS and 2MASS), using the full set of 105 colors. The method was not able to calculate the parameters for 597 965 objects, which will be discussed later in this section.

As an example, the derived stellar parameters and their associated uncertainties for a small set in our sample is presented in Appendix A (Table A.2), along with the corresponding photometric quality flag. A full version of the table is available online on VizierR.

As previously mentioned, the uncertainties were estimated by the standard deviation of the stellar parameters of neighboring reference objects. In cases where only one neighbor was available (i.e., only one comparison object fell within the defined neighborhood), the uncertainty was set to the average error of all objects with the same photometric quality and neighborhood. Our results show that stars with high-quality photometry (HQP subset) found at smaller neighborhood radii tend to exhibit smaller errors.

Table 2 summarizes how the nearly 5.6 million stars are grouped by their spectral types. The estimated T_{eff} were associated with a spectral type according to the semi-empirical relations by Pecaut & Mamajek (2013)¹⁸. As shown in the table, the majority of the sample consists of G, and K-type stars.

Figure 2 shows the distribution of the obtained stellar parameters in a Kiel diagram for the stars in our sample, color-coded by their estimated metallicities and separated by their neighborhood radius (see Sect. 3 for details). The distribution of results across neighborhoods, grouped by photometric quality, is summarized in Table A.3. The adopted reference data (both observational and synthetic) is also shown in gray.

It can be noted in Fig. 2 that for larger neighborhoods (5 or higher; six bottom panels), there are objects to which the method assigned stellar parameters that were not contemplated in the reference data. The majority of these 2913 stars, which represents 0.0005% of the sample with derived stellar parameters, is part of the SCP subset (97% of these objects) and the majority of them belongs to neighborhoods 9 and 10. The adoption of large neighborhood radii generated associations with reference stars with heterogeneous parameters, generating solutions with combinations of T_{eff} , $\log g$, and $[\text{Fe}/\text{H}]$ not present in the reference set.

Our method did not compute stellar parameters for 597 965 stars. We found that none of these objects had any counterparts in the reference dataset within any of the 10 neighborhood radii. Without any nearby reference star for photometric comparison, it was not possible to derive their parameters. Notably, 98% of them did not meet the photometric quality criteria. Their color indices fell well outside the typical range observed in stars with reliable parameter determinations. While most objects in

¹⁸ Available at https://www.pas.rochester.edu/~emamajek/EEM_dwarf_UBVIJHK_colors_Teff.txt.

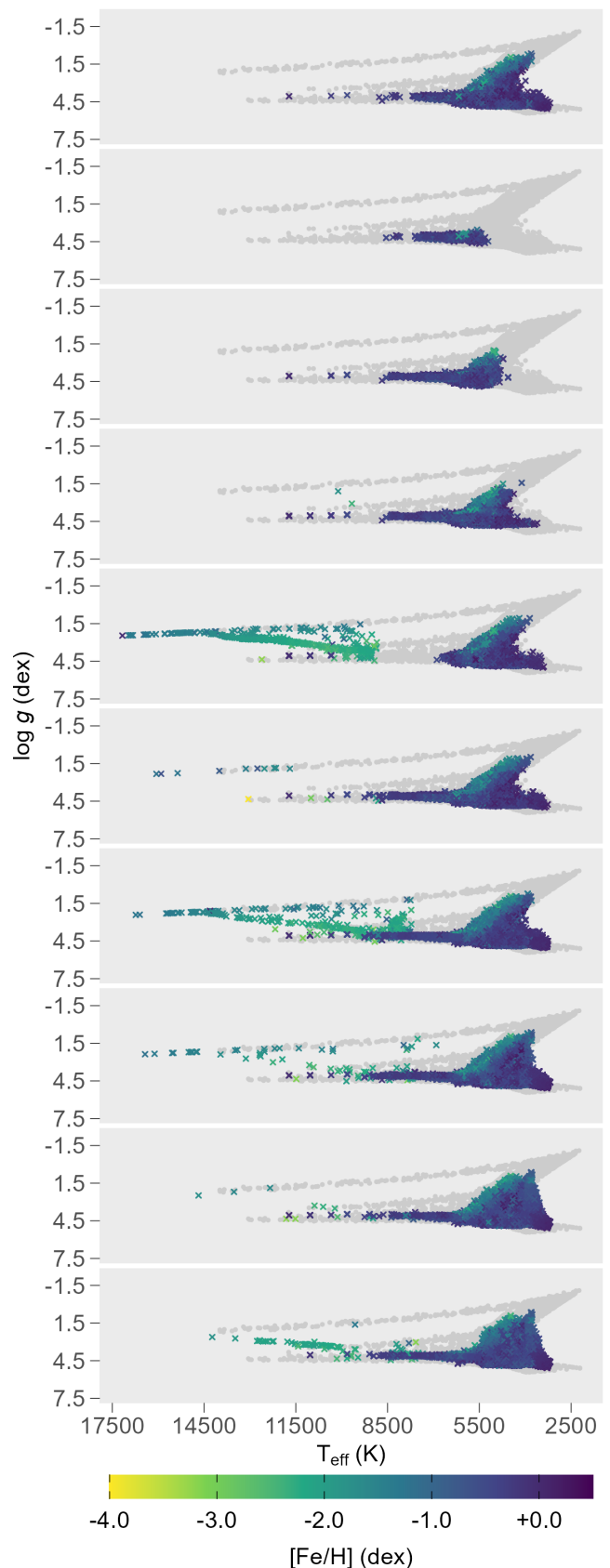


Fig. 2. Kiel diagrams showing the distribution of the nearly 5.6 million stars in our sample, separated by neighborhood. Panels are ordered from 1 (top panel) to 10 (bottom panel). The gray symbols represent the reference dataset. The color bar uses the same scale as in Fig. 1, and $[\text{Fe}/\text{H}]$ values range from -4.0 to $+0.324$ dex

Table 3. Table of statistics – median, median absolute deviation (MAD), and standard deviation (σ) – of differences between the estimated stellar parameters (T_{eff} , $\log g$, $[\text{Fe}/\text{H}]$) and literature values from the spectroscopic surveys LAMOST and APOGEE (validation dataset). Any reported statistical value (median, MAD, or sigma) with an absolute magnitude of 10^{-4} or lower was considered negligible and they are shown as zeros.

Neighbor- hood	N	ΔT_{eff} (K)			$\Delta \log g$ (dex)			$\Delta [\text{Fe}/\text{H}]$ (dex)		
		Median	MAD	σ	Median	MAD	σ	Median	MAD	σ
1	6436	0	0	103	0	0	0.151	0	0	0.082
2	7216	-1	93	106	-0.002	0.081	0.093	-0.001	0.131	0.148
3	56145	-17	103	124	-0.017	0.158	0.210	-0.002	0.146	0.167
4	47848	-35	115	141	-0.030	0.179	0.251	-0.011	0.188	0.210
5	20144	-16	116	136	-0.054	0.208	0.353	0.012	0.165	0.207
6	22136	-12	126	167	-0.054	0.192	0.373	0.011	0.192	0.243
7	45962	2	105	140	-0.092	0.238	0.441	0.020	0.199	0.234
8	5699	7	107	179	-0.022	0.150	0.401	0.031	0.276	0.304
9	4108	-3	133	201	-0.052	0.235	0.795	0	0.274	0.322
10	3947	15	147	214	-0.059	0.368	0.647	-0.052	0.257	0.298

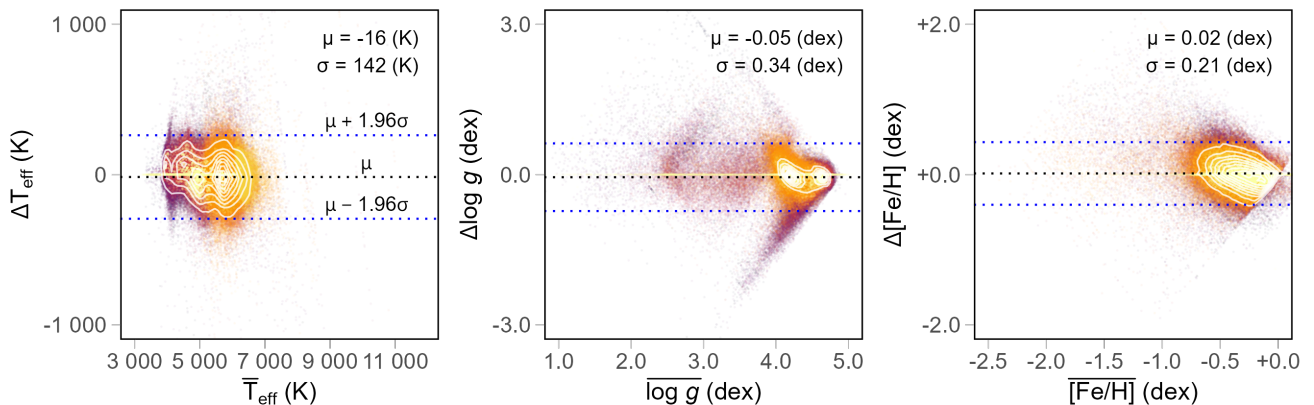


Fig. 3. Bland-Altman diagrams for T_{eff} (left panel), $\log g$ (middle panel), and $[\text{Fe}/\text{H}]$ (right panel), calculated using 105 colors, in comparison to values reported for the validation data. The black dotted horizontal line represents their mean difference and the blue dotted horizontal lines are the mean difference plus or minus 1.96σ to illustrate the confidence region. The color scheme represents the quality of the neighborhood proposed in our method, with yellow being the most reliable results (neighborhood 1) and red being the less reliable ones (neighborhood 10). The white contour lines are the densities calculated over the entire sample.

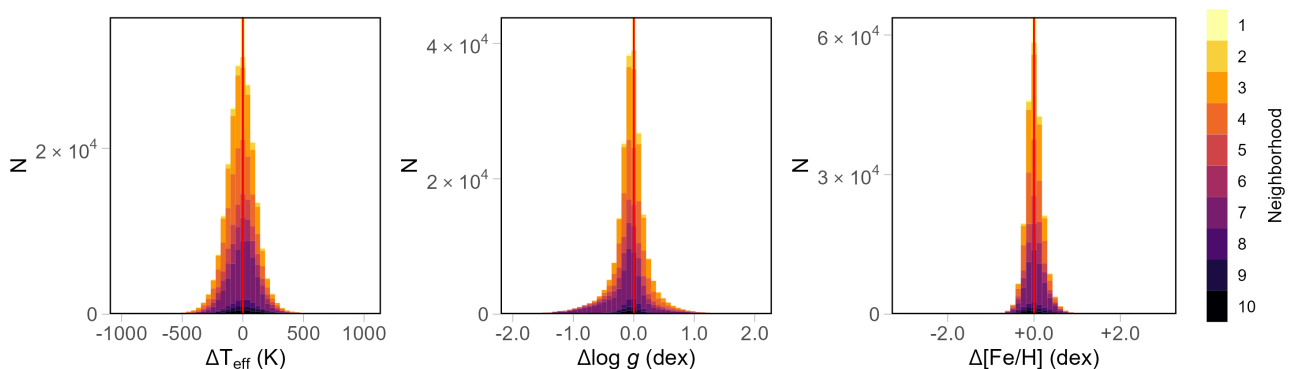


Fig. 4. Histograms of the differences of the stellar parameters estimated with 105 colors and the values reported for the validation data for T_{eff} (Left panel), $\log g$ (middle panel), and $[\text{Fe}/\text{H}]$ (right panel). The color scheme represents the different neighborhoods proposed in our method, with yellow being the most reliable results (neighborhood 1) and the less reliable ones (neighborhood 10). The red vertical line represents a null difference.

the sample have color values between -4.56 and 12 mag, these outliers exhibited values from -20.1 to 23.7 mag. Such extreme values lack physical interpretation, reinforcing that the method effectively rejects spurious detections.

4.2. Validation of our results

To assess the reliability of our method, we compared the estimated stellar parameters (T_{eff} , $\log g$, $[\text{Fe}/\text{H}]$) to those obtained from spectroscopy for the 219 641 objects (LAMOST and APOGEE) in our validation sample (see details in Sect. 2.3).

We quantified the differences between our estimates and our validation sample by computing the median, the median absolute deviation (MAD), and the standard deviation (σ).

Among them, MAD offers a robust measure of dispersion, as it is significantly less sensitive to outliers than, for example, the mean or the standard deviation. Although σ is widely used to describe variability in normally distributed data, it is known to be strongly influenced by extreme values. Nevertheless, we also report σ values due to its frequent use in the literature and because it is required for the Bland–Altman analysis described later in this section.

Table 3 reports statistics of ΔX ¹⁹ by neighborhood, which shows that the median of the differences in effective temperature (ΔT_{eff}) are quite small, having 35 K and 0 K as the maximum and the minimum absolute differences, respectively. Regarding the MAD of these differences, a value of 0 K was obtained for the smallest neighborhood radius and reached a maximum value of 147 K in the largest radius. $\Delta \log g$ presented values between -2.670×10^{-8} and -0.092 dex for the median, and a MAD between 1.923×10^{-7} and 0.368 dex, which were assigned to neighborhoods 1 and 10, respectively. It is worth mentioning that differences of the order of 10^{-4} or smaller were considered as zero in Table 3. $\Delta[\text{Fe}/\text{H}]$ medians have values also close to zero, with a maximum absolute difference of 0.052 dex. In this case, MAD values have a maximum of 0.276 dex in neighborhood 8.

These statistical results show that smaller neighborhoods (i.e., shorter radii) tend to produce stellar parameter estimates with lower dispersion. This effect is more pronounced for neighborhoods 5 and below across all parameters (T_{eff} , $\log g$, and $[\text{Fe}/\text{H}]$), with MAD values increasing with neighborhood radii. These findings suggest that smaller radii yield more reliable estimates, and thus, neighborhoods can be used as a proxy for the reliability of the derived parameters.

To recognize whether the difference between our results and those from spectroscopy presents a significant discrepancy, we adopted the Bland–Altman diagram. This diagram helps to assess the limits of agreement between two measurements (Haghighayegh et al. 2020). By definition, we adopted here the standard deviation to define a confidence region for the sample, which consists of taking data inside the range $\mu \pm 1.96\sigma$, where μ is the mean value. This helps to identify any systematic biases or random errors. Figure 3 shows that, for the three parameters under study, the vast majority of objects are found within the confidence region, suggesting that these parameters obtained in two different ways (the results obtained from spectroscopy and our method) are in good agreement. Considering the entire sample, we found that 96% of the differences in the effective temperature are inside the confidence region, with a σ equal to 142 K. In the case of $\log g$ and $[\text{Fe}/\text{H}]$, the 94 and 95% of the data are in the confidence region, with σ equal to 0.34 and 0.21 dex, respectively. These results have taken values associated with all neighborhoods.

As mentioned earlier, higher dispersion can be found at larger neighborhoods (see Table 3). This is related to the high radii values that had to be taken to estimate the stellar parameters. This is also illustrated in Fig. 4, where those objects with high dispersion are those with larger neighborhood values, which can be validated with the estimated MAD and σ values (Table 3). However, it is important to emphasize that they are a smaller subset compared to those with more reliable (closer) neighborhoods, equivalent to 37% of the validation data set. For

neighborhoods of 5 or less, the dispersion is smaller, with MAD of 71 K, 0.108 dex, and 0.104 dex, for T_{eff} , $\log g$, and $[\text{Fe}/\text{H}]$, respectively.

An important factor in this analysis is the behavior of the derived parameters for objects with high-quality photometry (HQP subset) and those that did not meet the quality criteria established in Sect. 2.1 (SCP subset), in order to validate whether this is an influential factor. The validation data contains 219 641 stars. Of these, 211 360 belong to the HQP subset, while the remaining 8 281 are part of the SCP group. For HQP stars, the median differences between our estimates and spectroscopic values were -14 K for ΔT_{eff} , -0.039 dex for $\Delta \log g$, and -0.001 dex for $\Delta[\text{Fe}/\text{H}]$. The corresponding MAD values were 73 K, 0.117 dex, and 0.115 dex, respectively.

The same statistical comparison was carried out for stars in the SCP subset. The results showed a slight increase in dispersion: the median differences were 61 K for ΔT_{eff} , 0.047 dex for $\Delta \log g$, and -0.096 dex for $\Delta[\text{Fe}/\text{H}]$, with corresponding MAD values of 107 K, 0.170 dex, and 0.136 dex, respectively.

Among SCP stars located in neighborhoods with value 5 or lower, the results exhibit even lower dispersion. The MAD values in this case were 106 K for ΔT_{eff} , 0.120 dex for $\Delta \log g$, and 0.109 dex for $\Delta[\text{Fe}/\text{H}]$, which are similar to those reported in Table 3.

These values indicate that our method is still capable of recovering reliable stellar parameters for objects that do not satisfy all photometric quality criteria, with a dispersion comparable to that obtained for the HQP subset.

One of the objectives of this work was to assess the reliability of the inferred stellar parameters for objects with somewhat compromised photometry. We have a low percentage ($\sim 4\%$) of this type of data in validation dataset, however, 66% of the sample with derived stellar parameters is part of the SCP subset. Therefore, a further discussion will be present in the next section concerning the parameter uncertainties for objects from the SCP subset compared to the results obtained by other works.

5. Discussion

5.1. Comparison with previous results

We compared our results with previous studies that analyzed J-PLUS data to estimate stellar atmospheric parameters such as T_{eff} , $\log g$, and $[\text{Fe}/\text{H}]$ using photometry. This comparison focuses on the works of Wang et al. (2022) and Huang et al. (2024), as introduced in Sect. 2.3.

We adopted the same approach to compare estimations by computing the differences between our estimates and those reported in these studies, using the full set of 105 colors. The comparison with Wang et al. (2022) yields a median difference of 6 K in T_{eff} and MAD of 76 K. The comparison with Huang et al. (2024) results in a median T_{eff} difference of 35 K and a MAD of 66 K.

Concerning $\log g$, the MAD values are 0.096 dex and 0.144 dex for the comparisons with Wang et al. (2022) and Huang et al. (2024), respectively. For $[\text{Fe}/\text{H}]$, the MAD values are 0.128 dex and 0.174 dex.

Table A.4 shows the statistics of all differences, separated by neighborhood and by photometric quality (HQP and SCP; see Sect. 2.1). In general, the differences found in T_{eff} for both samples, Wang et al. (2022) and Huang et al. (2024), are similar, which shows the capability of our method of deriving the stellar T_{eff} regardless of possible limitations in the J-PLUS photometry. Although higher differences are found for $\log g$ and $[\text{Fe}/\text{H}]$

¹⁹ Throughout this work, $\Delta X = X_{\text{our}} - X_{\text{spec}}$ for each parameter $X = T_{\text{eff}}$, $\log g$ or $[\text{Fe}/\text{H}]$.

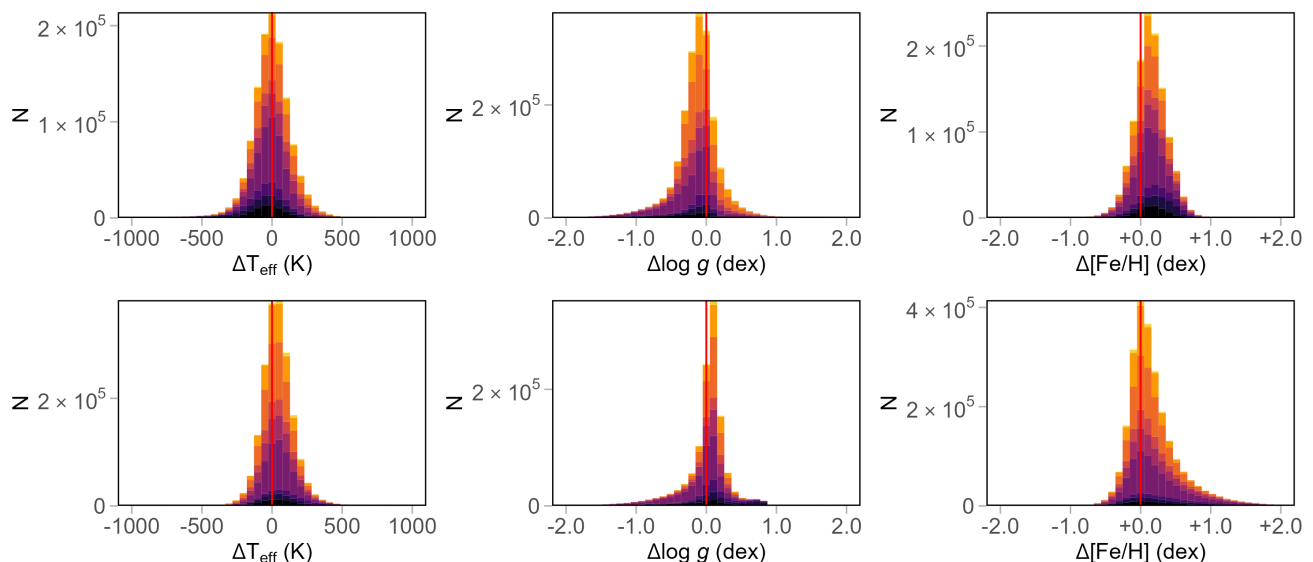


Fig. 5. Histograms of the differences in T_{eff} (left panels), $\log g$ (middle panels), and $[\text{Fe}/\text{H}]$ (right panels) between our results, obtained with 105 colors, and those from Wang et al. (2022) (top panels) and Huang et al. (2024) (bottom panels). Red vertical lines represent a null difference. The color bar is the same as the one shown in Fig. 4.

derived for the SCP sample with larger neighborhoods, the estimated values show less dispersion for smaller neighborhoods.

Figure 5 illustrates the differences mentioned above for the estimated parameters, color-coded by neighborhood, where darker colors represent larger neighborhoods. The highest dispersions are associated with objects in the largest neighborhoods. Based on the $\mu \pm 1.96\sigma$ criterion (see Sect. 4.2), 96% of the sample falls within the confidence interval for ΔT_{eff} in both comparison sets. For $\Delta \log g$, 94% of the stars are within the expected range, and for $\Delta[\text{Fe}/\text{H}]$, the coverage is 95% in both cases. These results indicate a good level of agreement between our estimated stellar parameters and those derived by Wang et al. (2022) and Huang et al. (2024).

Figure B.1 (Appendix B) compares the stellar atmospheric parameters estimated using our method based on 105 colors for 1 236 stars common to all datasets considered in this work: LAMOST, APOGEE, Wang et al. (2022), and Huang et al. (2024).

Linear regression analysis was used as a diagnostic tool to evaluate the agreement between our results and the reference datasets. The fits were computed using weighted least-squares (WLS), with the inverse squared uncertainties of the reference parameters as weights.

As previously observed, larger neighborhood values tend to result in greater dispersion in parameter estimates. In contrast, stars associated with neighborhood indices of 1 or 2 show tightly clustered distributions, suggesting more consistent and stable predictions in those regions. Linear regression analysis was performed to assess the reliability of the estimates. Reliable results are expected to yield correlation coefficients (R^2) near unity and intercepts close to zero. Comparisons with spectroscopic measurements (first and second rows) show regression slopes near one, confirming the consistency of our method with external reference data. The narrow confidence intervals of the fitted relations reflect the strong clustering of the data around the best-fit lines and the concentration of most stars within well-populated

regions of parameter space²⁰. The low RMSE values, reported in each panel, confirm the robustness of the agreement in the ranges of explored parameters. Comparisons with the photometric estimates of Wang et al. (2022) and Huang et al. (2024) (third and fourth rows) also exhibit high R^2 values for T_{eff} and $\log g$, with moderate correlations for $[\text{Fe}/\text{H}]$.

Our method estimates stellar parameters that agree with literature values of Wang et al. (2022) and Huang et al. (2024), and shows results of the same order, denoting low uncertainties. In contrast to those studies, our approach requires no previous training, which greatly reduces computation time. Moreover, our method does not produce spurious solutions. This is because we form clusters of stars with similar photometry (and hence similar atmospheric parameters) and restrict each solution to the chosen neighborhood radius. In this way, we only derive parameters for targets that have at least one reference star nearby in the color space. This ensures that the neighbors used have photometric and atmospheric properties consistent with the target star.

5.2. Color sample reduction

Reducing the number of photometric colors while maintaining the ability to estimate atmospheric parameters effectively would significantly speed up computations and enable the analysis of a larger sample – photometric surveys tend to have stars that do not have magnitudes available in all photometric bands. Many of the 105 colors used in our full model exhibit similar behavior with respect to stellar parameters and can be grouped accordingly. Appendix C (Fig. C.1) shows the correlation matrix of colors, illustrating this redundancy. We then applied the Principal Component Analysis (PCA), an algorithm that identifies correlated variables and reduces dimensionality.

Considering the eigenvalues, which represent the variance explained by each principal component, we defined a smaller subset of colors based on those that had similar loadings on the most significant components. The fact that colors with similar

²⁰ This subset is concentrated in $4500 \leq T_{\text{eff}} \leq 5000$, $4 \leq \log g \leq 5$, and $-0.5 \leq [\text{Fe}/\text{H}] \leq 0$

loadings exhibit similar behavior can be validated by a high correlation index between them.

The explained variance takes the largest values in the first four components with an explained cumulative variance of 96%. Considering these four components. The colors formed 11 groups of similar behavior, obtained by applying the Hartigan test to the estimated eigenvalues values for each color in the four PCA components.

We selected the color with the highest correlation index with respect to the other colors within each of the 11 groups. The 11 selected colors are $J0378 - J0660$, $J0395 - g$, $J0410 - J$, $J0430 - i$, $J0430 - z$, $g - K$, $J0660 - H$, $i - z$, $i - J$, $J0861 - z$, and $z - H$. The use of this reduced set expanded the number of analyzable stars to 6,539,507 (from the original pool of 7 400 214 after applying SExtractor's CLASS_STAR criterion; see Sect. 2.1). Stellar parameters were successfully derived for 6 045 593 stars. An increase of 397 107 objects compared to the 105 color set. Additionally, computation time decreased by more than 50%.

Figure 6 shows the distribution of parameter differences between results obtained with 105 and the reduced set of 11 colors. The left panels show the objects in the HQP subset, which present smaller differences between the parameters, in comparison to the SCP subset (right panels). The smallest discrepancies are observed for HQP stars in smaller neighborhoods. The median differences for the HQP subset are null for T_{eff} and $[\text{Fe}/\text{H}]$, and are equal to 0.002 dex for $\log g$. The SCP subset also shows minimal median differences in T_{eff} , with slightly larger deviations in $\log g$ and $[\text{Fe}/\text{H}]$, though all differences remain close to zero. Our results indicate that even after applying a significant dimensionality reduction and despite limitations in the photometric quality, we were able to recover similar derived stellar parameters.

For HQP stars, the MAD values are 39 K, 0.084 dex, and 0.064 dex for T_{eff} , $\log g$, and $[\text{Fe}/\text{H}]$, respectively. For SCP stars, these increase slightly to 50 K, 0.099 dex, and 0.086 dex.

It is worth emphasizing that these values were estimated considering all neighborhoods and that the differences between both samples are better noted when comparing individual neighborhoods.

Similar to trends on validation dataset, greater dispersion is seen at larger neighborhoods, especially in the SCP subset. For instance, the best-case scenario (HQP stars with neighborhood 1) yields MAD values of 0 K, 0 dex, and 0 dex for T_{eff} , $\log g$, and $[\text{Fe}/\text{H}]$, respectively. In contrast, the worst-case scenario (SCP stars with neighborhood 10) shows MAD values of 51 K, 0.211 dex, and 0.092 dex.

In summary, the applied color reduction has proven to be a good reference for stellar parameters, allowing a larger dataset to be analyzed, despite some increase in the derived uncertainties when compared to the results obtained with 105 colors and the validation data. This implementation generated a significant reduction in the required computational time compared to the time invested using 105 colors.

6. Conclusions

Although spectroscopy provides more direct parameter constraints, the extensive availability of photometric surveys offer a valuable alternative when spectroscopic data are not available. We estimated the atmospheric stellar parameters (T_{eff} , $\log g$, $[\text{Fe}/\text{H}]$) for a total of 5 648 486 stars in J-PLUS DR3, using 105 colors. In this work, we integrated photometric data from 12 J-PLUS bands and three 2MASS magnitudes. Differently from

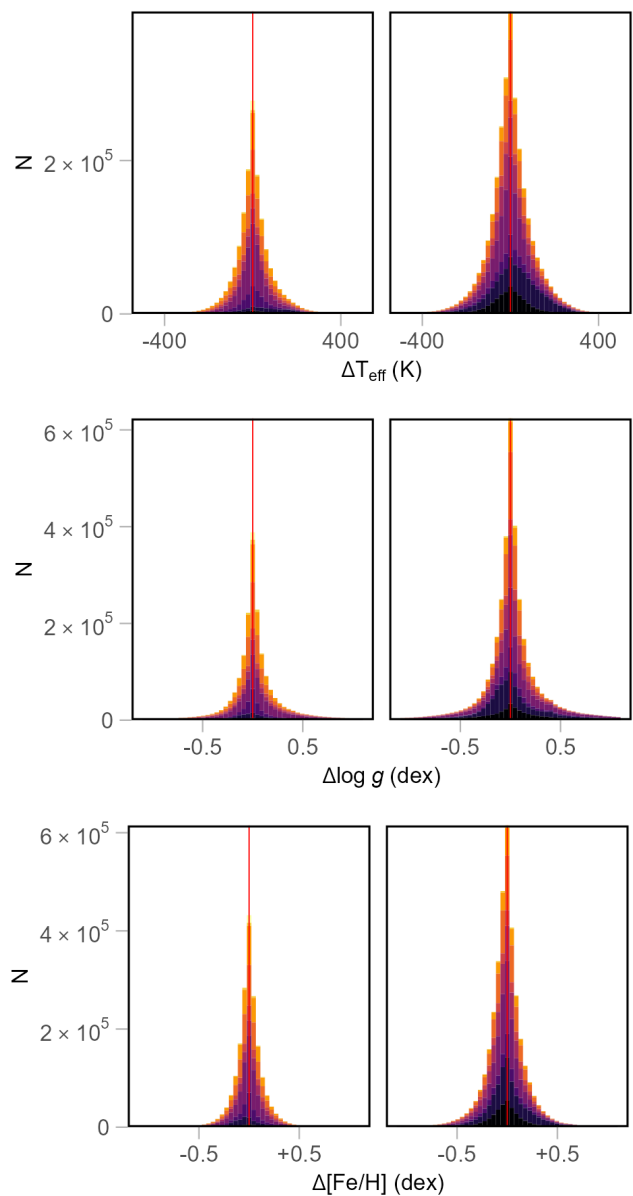


Fig. 6. Histograms of the differences in T_{eff} , $\log g$, and $[\text{Fe}/\text{H}]$, from top to bottom, respectively, obtained with our method using 105 colors and the results when using this same method with the 11 chosen colors. Left panels show the differences obtained for the HQP subset and right panels for those in the SCP subset. The color bar is the same as the one shown in Fig. 4.

previous studies with similar objectives using J-PLUS data, we incorporated near-infrared data to enhance parameter inference.

The adopted method was based on the k-means method combined with a modified KNN algorithm. Our approach consisted of a comparative analysis between reference datasets, comprising both observational data with spectroscopically derived atmospheric stellar parameters and synthetic data from models. As reference, we adopted data from LAMOST, APOGEE, and from the MIST models to infer T_{eff} , $\log g$, and $[\text{Fe}/\text{H}]$ for the objects in our sample. Our method is computationally efficient, avoiding overheads associated with training-intensive algorithms.

Considering all 105 colors, our results were in agreement with spectroscopic estimates from LAMOST and APOGEE. The estimated parameters were obtained not only for data with high-

quality photometry, but also for objects with somewhat compromised photometry.

This classification allowed for a systematic assessment of the robustness of our method across varying observational conditions. Our results demonstrate that the method yields reliable atmospheric parameters even when the photometric data are somewhat compromised.

The analysis showed that adopting different neighborhood radii enabled the determination of stellar parameters not only for objects with nearby reference data for which a small radius (neighborhood 1) was sufficient, but also for cases requiring progressively larger radii (up to neighborhood 10). A comparison with a validation dataset, as well as with results reported in the literature, indicated that the neighborhood size correlates with the reliability of our estimates. In particular, the most reliable parameters are generally obtained for neighborhoods with radii less than or equal to 5.

We reviewed the efficacy of using numerous color indices for parameter estimation, while exploring the possibility of identifying a smaller set of colors that could produce parameter estimates comparable in accuracy to those obtained from the complete set. Dimensionality reduction via principal component analysis (PCA) revealed that 11 selected colors retained the essential information required for parameter estimation. This reduced set of colors enabled the analysis of a larger number of stars, while reducing computational time. Despite minor increases in the estimated uncertainties, the reduced model maintains consistency with results from the full 105-color analysis.

Acknowledgements. J.A.'s contribution to this work is part of his academic activities as a professor at Universidad Militar Nueva Granada, Bogotá, Colombia. J.A., P.Cruz, E.S. acknowledge support from the Spanish Virtual Observatory (<https://svo.cab.inta-csic.es>) project funded by the Spanish Ministry of Science, Innovation and Universities /State Agency of Research MCIU/AEI/10.13039/501100011033 through grant PID2023-146210NB-I00. P.Cruz also acknowledges support from grant PID2019-107061GB-C61. P.Coelho acknowledges the support by Conselho Nacional de Desenvolvimento Científico e Tecnológico (Process 308715/2025-0). A.E. acknowledges the financial support from the Spanish Ministry of Science and Innovation and the European Union - NextGenerationEU through the Recovery and Resilience Facility project ICTS-MRR-2021-03-CEFCA. The work of V.M.P. is supported by NOIRLab, which is managed by the Association of Universities for Research in Astronomy (AURA) under a cooperative agreement with the U.S. National Science Foundation. A.A.C. acknowledges financial support from the Severo Ochoa grant CEX2021-001131-S funded by MCIN/AEI/10.13039/501100011033 and the project PID2023-153123NB-I00 funded by MCIN/AEI. Based on observations made with the JAST80 telescope and T80Cam camera for the J-PLUS project at the Observatorio Astrofísico de Javalambre (OAJ), in Teruel, owned, managed, and operated by the Centro de Estudios de Física del Cosmos de Aragón (CEFCA). We acknowledge the OAJ Data Processing and Archiving Unit (UPAD; [Cristóbal-Hornillos et al. 2012](#)) for reducing the OAJ data used in this work. Funding for the J-PLUS Project has been provided by the Governments of Spain and Aragón through the Fondo de Inversiones de Teruel; the Aragonese Government through the Research Groups E96, E103, E16_17R, E16_20R, and E16_23R; the Spanish Ministry of Science and Innovation (MCIN/AEI/10.13039/501100011033 y FEDER, Una manera de hacer Europa) with grants PID2021-124918NB-C41, PID2021-124918NB-C42, PID2021-124918NA-C43, and PID2021-124918NB-C44; the Spanish Ministry of Science, Innovation and Universities (MCIU/AEI/FEDER, UE) with grants PGC2018-097585-B-C21 and PGC2018-097585-B-C22; the Spanish Ministry of Economy and Competitiveness (MINECO) under AYA2015-66211-C2-1-P, AYA2015-66211-C2-2, AYA2012-30789, and ICTS-2009-14; and European FEDER funding (FCDD10-4E-867, FCDD13-4E-2685). The Brazilian agencies FINEP, FAPESP, and the National Observatory of Brazil have also contributed to this Project. This publication makes use of data products from the Two Micron All Sky Survey, which is a joint project of the University of Massachusetts and the Infrared Processing and Analysis Center/California Institute of Technology, funded by the National Aeronautics and Space Administration and the National Science Foundation. This research has made use of TOPCAT ([Taylor 2005](#)).

References

- Abazajian, K. N., Adelman-McCarthy, J. K., Agüeros, M. A., et al. 2009, *ApJS*, 182, 543
- Abdurro'uf, Accetta, K., Aerts, C., et al. 2022, *ApJS*, 259, 35
- Ahumada, R., Allende Prieto, C., Almeida, A., et al. 2020, *ApJS*, 249, 3
- Bai, Z.-R., Zhang, H.-T., Yuan, H.-L., et al. 2021, *Research in Astronomy and Astrophysics*, 21, 249
- Bailer-Jones, C. A. L., ed. 2008, *American Institute of Physics Conference Series*, Vol. 1082, CLASSIFICATION AND DISCOVERY IN LARGE ASTRONOMICAL SURVEYS: Proceedings of the International Conference: "Classification and Discovery in Large Astronomical Surveys"
- Bayo, A., Rodrigo, C., Barrado Y Navascués, D., et al. 2008, *A&A*, 492, 277
- Bishop, C. M. & Nasrabadi, N. M. 2007, *Journal of Electronic Imaging*, 16, 049901
- Bowen, I. S. & Vaughan, Jr., A. H. 1973, *Appl. Opt.*, 12, 1430
- Buder, S., Sharma, S., Kos, J., et al. 2021, *MNRAS*, 506, 150
- Cenarro, A. J., Moles, M., Cristóbal-Hornillos, D., et al. 2019, *A&A*, 622, A176
- Choi, J., Dotter, A., Conroy, C., et al. 2016, *ApJ*, 823, 102
- Coelho, P., Barbuy, B., Meléndez, J., Schiavon, R. P., & Castilho, B. V. 2005, *A&A*, 443, 735
- Cover, T. M. & Hart, P. E. 1967, *IEEE Transactions on Information Theory*, 13, 21
- Cristóbal-Hornillos, D., Gruel, N., Varela, J., et al. 2012, in *SPIE CS*, Vol. 8451
- Cruz, P., Aguilar, J. F., Garrido, H. E., Diaz, M. P., & Solano, E. 2022, *MNRAS*, 515, 1416
- Cui, X.-Q., Zhao, Y.-H., Chu, Y.-Q., et al. 2012, *Research in Astronomy and Astrophysics*, 12, 1197
- Deng, L.-C., Newberg, H. J., Liu, C., et al. 2012, *Research in Astronomy and Astrophysics*, 12, 735
- Dotter, A. 2016, *ApJS*, 222, 8
- Everitt, B. 1995, *Bmj*, 311, 535
- Gaia Collaboration, Brown, A. G. A., Vallenari, A., et al. 2018, *A&A*, 616, A1
- Gaia Collaboration, Brown, A. G. A., Vallenari, A., et al. 2021, *A&A*, 649, A1
- Gaia Collaboration, Prusti, T., de Bruijne, J. H. J., et al. 2016, *A&A*, 595, A1
- Galarza, C. A., Daflon, S., Placco, V. M., et al. 2022, *A&A*, 657, A35
- Garrido, H. E., Cruz, P., Diaz, M. P., & Aguilar, J. F. 2019, *MNRAS*, 482, 5379
- Green, G. M. 2018, *The Journal of Open Source Software*, 3, 695
- Gunn, J. E., Siegmund, W. A., Mannery, E. J., et al. 2006, *AJ*, 131, 2332
- Haghayegh, S., Kang, H.-A., Khoshnevis, S., Smolensky, M. H., & Diller, K. R. 2020, *Physiological Measurement*, 41, 055012
- Hartigan, J. A. 1975, *Clustering Algorithms*, NSF Award Number 7508374. Directorate for Computer and Information Science and Engineering, Division of Computing and Communication Foundations. 1975.
- Hojnacki, S. M., Kastner, J. H., Micela, G., Feigelson, E. D., & LaLonde, S. M. 2007, *ApJ*, 659, 585
- Huang, Y., Beers, T. C., Xiao, K., et al. 2024, *ApJ*, 974, 192
- Husser, T. O., Wende-von Berg, S., Dreizler, S., et al. 2013, *A&A*, 553, A6
- Jain, A. K. & Dubes, R. C. 1988, *Algorithms for clustering data* (Prentice-Hall, Inc.)
- Jönsson, H., Holtzman, J. A., Allende Prieto, C., et al. 2020, *AJ*, 160, 120
- Kurucz, R. L. 1970, *SAO Special Report*, 309
- Kurucz, R. L. 1979, *ApJS*, 40, 1
- Kurucz, R. L. 1993, *SYNTHES spectrum synthesis programs and line data*
- Lee, Y. S., Beers, T. C., Sivarani, T., et al. 2008a, *AJ*, 136, 2022
- Lee, Y. S., Beers, T. C., Sivarani, T., et al. 2008b, *AJ*, 136, 2050
- López-Sanjuan, C., Vázquez Ramió, H., Varela, J., et al. 2019, *A&A*, 622, A177
- López-Sanjuan, C., Vázquez Ramió, H., Xiao, K., et al. 2024, *A&A*, 683, A29
- López-Sanjuan, C., Yuan, H., Vázquez Ramió, H., et al. 2021, *A&A*, 654, A61
- Luo, A. L., Zhao, Y.-H., Zhao, G., et al. 2015, *Research in Astronomy and Astrophysics*, 15, 1095
- Luo, A. L., Zhao, Y. H., Zhao, G., & et al. 2022, *VizieR Online Data Catalog: LAMOST DR7 catalogs (Luo+., 2019)*, *VizieR On-line Data Catalog: V/156*. Originally published in: 2019RAA...in.prep..L
- Mendes de Oliveira, C., Ribeiro, T., Schoenell, W., et al. 2019, *MNRAS*, 489, 241
- Morales-Luis, A. B., Sánchez Almeida, J., Aguerri, J. A. L., & Muñoz-Tuñón, C. 2011, *ApJ*, 743, 77
- Paxton, B., Bildsten, L., Dotter, A., et al. 2011, *ApJS*, 192, 3
- Paxton, B., Cantiello, M., Arras, P., et al. 2013, *ApJS*, 208, 4
- Paxton, B., Marchant, P., Schwab, J., et al. 2015, *ApJS*, 220, 15
- Pecaut, M. J. & Mamajek, E. E. 2013, *ApJS*, 208, 9
- Quispe-Huaynasi, F., Roig, F., Daflon, S., et al. 2023, *MNRAS*, 522, 3898
- R Core Team. 2018, *R: A Language and Environment for Statistical Computing*, R Foundation for Statistical Computing, Vienna, Austria
- Sánchez Almeida, J. & Allende Prieto, C. 2013, *ApJ*, 763, 50
- Schlegel, D. J., Finkbeiner, D. P., & Davis, M. 1998, *ApJ*, 500, 525
- Skrutskie, M. F., Cutri, R. M., Stiening, R., et al. 2006, *AJ*, 131, 1163
- Sprague, D., Culhane, C., Kounkel, M., et al. 2022a, *AJ*, 163, 152

- Sprague, D., Culhane, C., Kounkel, M., et al. 2022b, *VizieR Online Data Catalog*, J/AJ/163/152
- Taylor, M. 2011, preprint (record ascl: 1101.010)
- Taylor, M. B. 2005, in *Astronomical Society of the Pacific Conference Series*, Vol. 347, *Astronomical Data Analysis Software and Systems XIV*, ed. P. Shopbell, M. Britton, & R. Ebert, 29
- Wang, C., Bai, Y., Yuan, H., et al. 2022, *A&A*, 664, A38
- Whitten, D. D., Placco, V. M., Beers, T. C., et al. 2019, *A&A*, 622, A182
- Wilson, J. C., Hearty, F., Skrutskie, M. F., et al. 2010, in *Society of Photo-Optical Instrumentation Engineers (SPIE) Conference Series*, Vol. 7735, *Ground-based and Airborne Instrumentation for Astronomy III*, ed. I. S. McLean, S. K. Ramsay, & H. Takami, 77351C
- Wilson, J. C., Hearty, F. R., Skrutskie, M. F., et al. 2019, *PASP*, 131, 055001
- Yang, L., Yuan, H., Xiang, M., et al. 2022, *A&A*, 659, A181
- Yanny, B., Rockosi, C., Newberg, H. J., et al. 2009, *AJ*, 137, 4377
- York, D. G., Adelman, J., Anderson, Jr., J. E., et al. 2000, *AJ*, 120, 1579
- Yuan, H. B., Liu, X. W., & Xiang, M. S. 2013, *MNRAS*, 430, 2188
- Zasowski, G., Johnson, J. A., Frinchaboy, P. M., et al. 2013, *AJ*, 146, 81

Appendix A: Additional material

Table A.1 shows the distribution of the reference data in each of the 19 clusters suggested by the Hartigan test implementation. The first and second columns shows the cluster number and the source, respectively. The third column indicates the number of objects (observed or synthetic) within each cluster. The remaining columns shows the minimum, the maximum, and the median values of T_{eff} , $\log g$, and $[\text{Fe}/\text{H}]$, respectively, as the summary of the distribution. A detailed information is given in Sect. 3.

Table A.2 summarizes the estimated stellar atmospheric parameters (T_{eff} , $\log g$, $[\text{Fe}/\text{H}]$) calculated using our method with 105 and 11 colors. The first column lists the J-PLUS names of each object. The second and third columns show their corresponding J2000 equatorial coordinates. Columns from four to nine show the stellar parameters estimated using our method with 105 colors and their corresponding errors. Columns 12 to 17 report the same parameters estimated using 11 colors and their errors. Columns 10 and 18 report the neighborhood values assigned by our method, and columns 11 and 19 indicate the number of stars from the reference dataset used to calculate the stellar parameters, for 105 and 11 colors (N_{ref}), respectively. Column 20 reports the photometric quality subset of the object (see Sect. 2.1 for details). The complete version of this table, with the derived parameters for the almost five million objects, is available online in Vizier²¹.

Table A.3 presents the statistics of the obtained stellar parameters using 105 colors, distributed according to their neighborhood radius and grouped according their photometric quality. The first column indicates the photometric quality subset. The second column shows the different neighborhood values, from 1 to 10. The third column indicates the number of stars with stellar parameters estimated according to their neighborhood radius. The remaining columns show the statistics (median, MAD, σ , minimum and maximum values) obtained for each stellar parameter.

Table A.4 shows the differences (Δ) obtained between our estimated stellar parameters and those from Wang et al. (2022) and Huang et al. (2024), discriminated by the photometric quality samples and the different neighborhoods. The first column shows the two subsets with different photometric quality. The second column indicates the neighborhood values using 105 colors. The remaining columns report the statistics (median, MAD, σ) for each Δ value.

Appendix B: Comparison of estimated atmospheric parameters

Figure B.1 shows the comparison of stellar atmospheric parameters (T_{eff} , $\log g$, and $[\text{Fe}/\text{H}]$) derived in this work using the 105-color method and those reported in the literature for 1 236 stars in common among all surveys. The comparison includes spectroscopic parameters from APOGEE (Sprague et al. 2022a) and LAMOST DR9 (Bai et al. 2021), as well as photometric estimates from Wang et al. (2022) and Huang et al. (2024) based on J-PLUS DR2 and DR3 data, respectively. A linear regression was applied to each panel as a diagnostic tool to assess the agreement between our estimates and the reference values. The dashed line represents the linear relationship of best fit, while the shaded region corresponds to the 95% confidence interval of the fit. The regression equation, coefficient of determination

(R^2), and root mean square error (RMSE) are presented for each panel.

Appendix C: Correlation matrix between colors and stellar parameters

Matrix of correlations with colors between the parameters Temperature, Gravity and Metallicity and the 105 colors extracted from the information collected from J-PLUS and 2MASS survey. On one side, there is a colored bar associated with the correlation index for each of the cases. The order of the variables in the array viewed from top to bottom and left to right is: T_{eff} , $\log g$, $[\text{Fe}/\text{H}]$, $u - J0378$, $u - J0395$, $u - J0410$, $u - J0430$, $u - g$, $u - J0515$, $u - r$, $u - J0660$, $u - i$, $u - J0861$, $u - z$, $u - J$, $u - H$, $u - K$, $J0378 - J0395$, $J0378 - J0410$, $J0378 - J0430$, $J0378 - g$, $J0378 - J0515$, $J0378 - r$, $J0378 - J0660$, $J0378 - i$, $J0378 - J0861$, $J0378 - z$, $J0378 - J$, $J0378 - H$, $J0378 - K$, $J0395 - J0410$, $J0395 - J0430$, $J0395 - g$, $J0395 - J0515$, $J0395 - r$, $J0395 - J0660$, $J0395 - i$, $J0395 - J0861$, $J0395 - z$, $J0395 - J$, $J0395 - H$, $J0395 - K$, $J0410 - J0430$, $J0410 - g$, $J0410 - J0515$, $J0410 - r$, $J0410 - J0660$, $J0410 - i$, $J0410 - J0861$, $J0410 - z$, $J0410 - J$, $J0410 - H$, $J0410 - K$, $J0430 - g$, $J0430 - J0515$, $J0430 - r$, $J0430 - J0660$, $J0430 - i$, $J0430 - J0861$, $J0430 - z$, $J0430 - J$, $J0430 - H$, $J0430 - K$, $g - J0515$, $g - r$, $g - J0660$, $g - i$, $g - J0861$, $g - z$, $g - J$, $g - H$, $g - K$, $J0515 - r$, $J0515 - J0660$, $J0515 - i$, $J0515 - J0861$, $J0515 - z$, $J0515 - J$, $J0515 - H$, $J0515 - K$, $r - J0660$, $r - i$, $r - J0861$, $r - z$, $r - J$, $r - H$, $r - K$, $J0660 - i$, $J0660 - J0861$, $J0660 - z$, $J0660 - J$, $J0660 - H$, $J0660 - K$, $i - J0861$, $i - z$, $i - J$, $i - H$, $i - K$, $J0861 - z$, $J0861 - J$, $J0861 - H$, $J0861 - K$, $z - J$, $z - H$, $z - K$, $J - H$, $J - K$, $H - K$.

²¹ <https://vizier.cds.unistra.fr>

Table A.1. Distribution of the reference sample into 19 clusters. The summary of their stellar parameters is given by the minimum (Min), the maximum (Max), and the median values within each group.

Cluster	Source	N	T_{eff} (K)			$\log g$ (dex)			[Fe/H] (dex)		
			Min	Max	Median	Min	Max	Median	Min	Max	Median
1	LAMOST	4	5742	11720	8339	4.029	4.388	4.123	-0.44	-0.026	-0.174
1	MIST	290	7968	18766	10277	1.099	4.554	3.461	-4	0.5	-2
2	APOGEE	880	3186	4645	3815	0.652	5.067	4.655	-1.435	0.303	-0.054
	LAMOST	572	3744	5988	3952	1.084	4.897	4.596	-1.387	-0.001	-0.388
	MIST	2568	2212	4661	3553	-1.093	5.416	0.243	-4	0.5	-0.75
	MIST	3	167112	168845	167740	6.812	6.972	6.882	-3	-1.75	-2
4	MIST	38	99452	108156	103784	5.501	7.355	6.375	-4	0.5	-0.625
5	MIST	52	89612	98827	93157	5.201	7.608	6.969	-4	0.5	-0.875
6	MIST	22	128097	138551	131921	5.958	7.390	6.741	-3	0	-1.375
7	APOGEE	953	4560	6305	5517	2.070	4.595	4.200	-1.589	0.295	-0.272
	LAMOST	5457	4888	6889	5760	1.805	4.890	4.250	-2.441	0.03	-0.33
	MIST	522	4629	6034	5173	0.126	4.957	2.392	-4	0.5	-1.5
8	MIST	10	151161	161093	156536	6.325	6.985	6.657	-3	0.5	-1.375
9	MIST	162	17003	33645	26547	2.351	7.972	5.614	-4	0.5	-1.25
10	MIST	10	140204	149902	145439	6.441	7.295	6.746	-3	0.5	-1
11	APOGEE	2932	3956	5558	4822	0.952	4.753	3.975	-1.945	0.324	-0.188
	LAMOST	3998	3852	6355	4804	0.932	4.900	4.618	-2.41	0.059	-0.288
	MIST	676	3933	5464	4547	0.059	5.419	2.063	-4	0.5	-1.25
12	MIST	38	118267	127575	123348	5.672	7.340	6.600	-4	0.5	-0.75
13	MIST	88	38183	59578	52855	3.818	7.899	7.534	-4	0.5	-0.875
14	MIST	34	109044	117759	113214	5.649	7.389	6.942	-4	0.25	-1.25
15	MIST	135	29174	48434	38556	3.239	7.925	4.128	-4	0.5	-1.25
16	MIST	63	46983	79817	74664	3.980	7.663	5.220	-4	0.5	-0.75
17	APOGEE	3	4843	6002	5765	3.700	4.241	4.099	-0.807	-0.098	-0.613
	LAMOST	756	4813	9820	6441	3.359	4.468	4.158	-2.301	0.001	-0.363
	MIST	654	5402	8622	6501	0.364	4.774	3.802	-4	0.5	-1.75
18	MIST	66	80363	89401	84705	5.048	7.708	6.972	-4	0.5	-1.25
19	MIST	79	46637	69723	64639	4.026	7.791	4.852	-4	0.5	-0.5

Table A.2. Stellar parameters estimated using the complete and the reduced sets with 105 and 11 colors, respectively. The columns are described in the text. The complete version of this table is available online on Vizier.

J-PLUS-ID	RA (deg)	Dec (deg)	$T_{\text{eff},105}$ (K)	$\sigma_{T_{\text{eff},105}}$ (K)	$\log g_{105}$ (dex)	$\sigma_{\log g_{105}}$ (dex)	[Fe/H] ₁₀₅ (dex)	$\sigma_{\text{Fe}/\text{H}_{105}}$ (dex)	Neighbor- hood ₁₀₅	$N_{\text{ref},105}$	$T_{\text{eff},11}$ (K)	$\sigma_{T_{\text{eff},11}}$ (K)	$\log g_{11}$ (dex)	$\sigma_{\log g_{11}}$ (dex)	[Fe/H] ₁₁ (dex)	$\sigma_{\text{Fe}/\text{H}_{11}}$ (dex)	Neighbor- hood ₁₁	$N_{\text{ref},11}$	Quality sample
100003-1000	38.37844	6.79366	3930	208	4.489	0.635	-0.239	0.281	9	1217	3900	109	4.632	0.307	-0.029	0.207	5	1	SCP
100003-1005	37.89399	7.35927	5310	140	4.384	0.304	-0.307	0.181	4	76	5224	101	4.069	0.168	-0.295	0.132	2	1	HQP
100003-10091	37.83760	7.36556	3586	215	4.662	0.274	-0.039	0.095	9	245	3456	113	4.721	0.252	-0.036	0.073	5	23	SCP
100003-10107	38.25897	7.35027	4597	109	4.549	0.273	-0.152	0.163	7	200	4592	106	4.299	0.701	-0.110	0.151	9	108	HQP
100003-10144	38.98693	7.36944	3477	115	4.716	0.234	-0.010	0.081	9	108	3532	350	4.502	0.359	-0.048	0.101	8	3	SCP
100003-10149	38.16998	7.36824	5623	132	4.276	0.163	-0.400	0.189	4	50	5649	92	4.256	0.095	-0.378	0.191	3	7	SCP
100003-10182	37.82243	7.37248	3983	181	4.515	0.544	-0.267	0.282	9	1043	3832	97	1.625	2.114	-1.325	0.717	6	220	SCP
100003-10187	39.12102	7.36652	5989	178	4.167	0.152	-0.457	0.210	3	32	6055	168	4.198	0.226	-0.373	0.196	2	12	HQP
100003-10189	37.99008	7.35945	5584	77	4.332	0.228	-0.032	0.144	3	10	5573	78	4.315	0.240	-0.072	0.150	2	8	HQP
100003-10203	38.79858	7.37208	4942	123	4.691	0.302	-0.013	0.073	9	181	3415	177	4.347	0.858	-0.018	0.171	5	2	SCP
100003-10223	38.79858	7.37208	4942	123	4.691	0.302	-0.013	0.073	9	181	3415	177	4.347	0.858	-0.018	0.171	5	2	SCP
100003-10229	38.94176	7.37336	4395	108	4.598	0.276	-0.141	0.207	7	79	4400	118	4.618	0.052	-0.061	0.107	7	3	HQP
100003-10245	38.13169	7.37494	3864	153	4.727	0.409	-0.896	0.228	9	1	3546	122	4.851	0.530	-0.090	0.217	9	1	SCP
100003-10288	38.20622	7.37929	4964	118	3.280	0.729	-0.513	0.208	7	125	4978	119	3.412	0.723	-0.474	0.172	9	229	HQP
100003-10294	38.42641	7.37885	4245	113	4.698	0.255	-0.200	0.164	6	1	4302	126	4.649	0.098	-0.279	0.164	3	26	HQP
100003-10298	38.26707	7.37358	4260	120	4.617	0.099	-0.117	0.152	7	69	4242	36	4.642	0.071	-0.049	0.077	3	3	HQP
100003-10304	38.06631	7.37158	5758	47	4.173	0.098	-0.339	0.132	3	9	5750	119	4.249	0.247	-0.398	0.125	2	7	HQP
100003-10309	37.93113	7.37490	3714	145	4.616	0.306	-0.064	0.089	8	129	3699	135	4.638	0.256	-0.064	0.091	4	96	HQP
100003-10332	38.77928	7.35694	6130	80	4.238	0.075	-0.484	0.090	6	5	6227	180	4.179	0.115	-0.346	0.184	4	151	SCP
100003-10336	38.33761	7.38360	3733	121	4.130	0.235	-0.128	0.236	8	1	3733	143	4.130	0.267	-0.128	0.249	4	1	SCP
100003-10348	38.27514	7.38509	3641	162	4.473	0.297	-0.098	0.126	9	7	3501	46	4.424	0.105	-0.051	0.098	5	2	SCP
100003-10352	38.05742	7.38375	3881	121	4.577	0.235	-0.415	0.236	8	1	3881	143	4.577	0.267	-0.415	0.249	4	1	SCP
100003-10360	39.01297	7.38443	4838	105	3.896	1.281	-0.528	0.021	7	2	4741	97	2.899	0.832	-0.515	0.143	9	12	SCP
100003-10388	38.84196	7.38046	5620	81	4.151	0.272	-0.234	0.163	3	5	5556	122	4.128	0.160	-0.283	0.141	2	5	HQP
100003-10399	38.15408	7.38761	5485	139	4.015	0.488	-1.099	0.669	6	3	5398	276	3.534	0.790	-1.004	0.584	4	64	SCP
100003-10420	38.86485	7.35709	6401	201	4.158	0.095	-0.461	0.362	7	517	6481	213	4.152	0.104	-0.481	0.370	8	139	SCP
100003-10430	38.50724	7.38084	5871	87	4.205	0.143	-0.519	0.140	3	41	5849	81	4.191	0.156	-0.604	0.156	2	25	HQP
100003-10466	38.15998	7.39121	3888	142	4.614	0.153	-0.295	0.258	9	108	4090	117	4.662	0.515	-0.122	0.267	6	1	SCP
100003-10506	38.81393	7.39422	4719	70	4.772	0.103	-0.450	0.425	8	2	4771	112	3.980	0.918	-0.316	0.198	10	463	SCP
100003-10515	38.51547	7.38997	5690	111	4.210	0.223	-0.427	0.182	3	12	5675	142	4.171	0.210	-0.454	0.205	2	9	HQP
100003-10519	37.91129	7.39526	5776	445	3.867	0.350	-1.454	0.237	9	2	—	—	—	—	—	—	—	—	SCP
100003-10523	38.64669	7.39100	4967	98	4.484	0.236	0.050	0.133	5	1	4889	85	3.462	0.334	-0.133	0.024	7	3	HQP
100003-10541	37.86663	7.38977	3763	19	4.764	0.091	-0.064	0.132	6	2	3732	58	4.690	0.090	-0.025	0.089	3	5	HQP
100003-10556	38.31917	7.38267	4877	112	4.267	0.551	-0.086	0.154	7	156	4876	86	4.299	0.503	0.020	0.109	9	20	SCP
100003-10559	38.62032	7.39626	5232	113	4.218	0.479	-0.175	0.194	7	113	5255	103	4.420	0.337	-0.190	0.161	9	99	HQP
100003-10564	38.22547	7.38638	3933	90	4.627	0.111	-0.243	0.429	7	14	3934	91	4.601	0.135	-0.275	0.298	4	261	HQP
100003-10566	38.48288	7.39844	4887	88	4.214	0.780	-0.391	0.110	6	4	4970	60	3.774	0.594	-0.410	0.059	8	3	SCP
100003-10603	38.25412	7.40170	5272	287	3.156	0.513	-1.455	0.567	6	12	5173	122	2.836	0.530	-1.582	0.217	9	1	SCP
100003-10611	38.67809	7.39763	5155	153	4.600	0.255	-0.363	0.164	6	1	5197	99	4.781	0.421	-0.292	0.119	7	1	HQP
100003-1064	39.13597	6.79789	5462	153	3.620	0.409	-1.286	0.228	9	1	—	—	—	—	—	—	—	—	SCP

Table A.3. Statistics for the objects assigned to each neighborhood and according to their photometric quality (HQP or SCP).

Quality sample	Neighborhood	N	T_{eff} (K)			$\log g$ (dex)			[Fe/H] (dex)								
			median	MAD	σ	min.	max.	median	MAD	σ	min.	max.					
HQP	1	15491	5177	787	736	3186	11720	4.317	0.378	0.637	0.652	5.067	-0.281	0.267	0.300	-2.441	0.324
	2	24302	6354	136	194	5210	8544	4.172	0.050	0.062	3.700	4.653	-0.346	0.129	0.212	-2.301	0.056
	3	323418	5730	267	321	4560	11720	4.224	0.117	0.172	2.037	4.890	-0.273	0.193	0.224	-2.441	0.295
	4	392880	5632	257	304	3669	11720	4.231	0.106	0.210	1.501	4.900	-0.296	0.203	0.249	-2.441	0.299
	5	142215	5111	411	467	3391	15784	4.314	0.371	0.571	1.109	5.002	-0.224	0.232	0.276	-2.518	0.324
	6	186845	5058	452	556	3267	9820	4.333	0.348	0.538	0.985	4.998	-0.231	0.229	0.264	-2.431	0.324
	7	510792	4700	497	496	3253	14068	4.470	0.270	0.516	0.731	5.037	-0.219	0.172	0.207	-2.410	0.324
	8	174394	3881	258	373	3186	11033	4.613	0.065	0.325	0.652	5.067	-0.184	0.205	0.214	-2.410	0.324
	9	101152	3945	458	504	3186	11720	4.596	0.115	0.432	0.918	5.067	-0.220	0.157	0.201	-2.410	0.304
	10	42106	4462	334	380	3237	11155	4.514	0.239	0.499	0.932	4.954	-0.324	0.163	0.191	-2.410	0.304
SCP	1	4	6364	85	1215	3958	6430	4.279	0.076	0.173	4.208	4.590	-0.275	0.128	0.133	-0.445	-0.122
	2	20457	6358	144	203	5309	8544	4.172	0.054	0.064	3.544	4.665	-0.334	0.139	0.221	-2.301	0.001
	3	240658	5803	331	380	4560	11720	4.206	0.104	0.162	2.037	4.890	-0.293	0.199	0.274	-2.441	0.295
	4	595710	5685	264	338	3606	11720	4.227	0.107	0.193	1.427	4.849	-0.334	0.218	0.270	-2.441	0.295
	5	220049	5567	351	513	3466	17169	4.259	0.214	0.442	1.060	4.917	-0.338	0.274	0.323	-3.225	0.324
	6	469090	5602	346	479	3314	16056	4.229	0.143	0.357	0.985	4.998	-0.387	0.250	0.325	-4.000	0.324
	7	801559	5111	522	611	3267	16731	4.247	0.326	0.491	0.731	5.037	-0.324	0.231	0.287	-3.081	0.324
	8	265713	4154	802	890	3186	16428	4.563	0.187	0.507	0.652	5.067	-0.331	0.308	0.336	-3.127	0.324
	9	671631	3954	433	678	3186	14679	4.560	0.137	0.410	0.652	5.067	-0.251	0.214	0.252	-3.194	0.324
	10	450020	4802	492	579	3186	14233	4.299	0.446	0.523	0.652	5.067	-0.360	0.175	0.227	-3.167	0.324

Table A.4. Statistics of the differences between our derived stellar parameters using 105 colors and those from Wang et al. (2022) and Huang et al. (2024) (comparison dataset), separated by the quality of their photometry and the proposed neighborhood values.

Quality sample	Neighbor-hood	ΔT_{eff} (K)			$\Delta \log g$ (dex)			$\Delta[\text{Fe}/\text{H}]$ (dex)		
		median	MAD	σ	median	MAD	σ	median	MAD	σ
<i>Comparison with Wang et al. (2022)</i>										
HQP	1	-42	126	155	0.071	0.195	0.310	0.051	0.177	0.193
	2	79	126	137	0.113	0.050	0.063	0.114	0.137	0.161
	3	4	111	130	0.098	0.100	0.158	0.094	0.139	0.159
	4	-10	106	124	0.081	0.086	0.170	0.107	0.157	0.177
	5	-19	116	131	0.054	0.214	0.368	0.081	0.165	0.194
	6	-17	112	129	0.043	0.178	0.386	0.093	0.167	0.192
	7	-9	86	95	0.003	0.166	0.372	0.107	0.148	0.177
	8	-13	85	94	0.059	0.088	0.282	0.222	0.225	0.233
	9	-7	112	116	0.048	0.157	0.445	0.117	0.236	0.244
	10	-14	91	98	0.029	0.150	0.382	0.060	0.143	0.163
SCP	1	118	126	140	0.135	0.064	0.055	0.153	0.053	0.053
	2	108	139	144	0.111	0.055	0.068	0.126	0.161	0.188
	3	40	130	151	0.097	0.101	0.156	0.133	0.181	0.205
	4	41	121	143	0.076	0.098	0.179	0.193	0.192	0.214
	5	39	137	159	0.080	0.168	0.304	0.179	0.227	0.254
	6	39	130	155	0.065	0.130	0.278	0.206	0.229	0.266
	7	6	106	136	0.000	0.208	0.406	0.164	0.199	0.249
	8	-8	132	230	0.075	0.160	0.436	0.192	0.265	0.305
	9	-19	129	279	0.040	0.236	0.547	0.179	0.242	0.270
	10	-27	112	154	-0.119	0.429	0.526	0.177	0.196	0.220
<i>Comparison with Huang et al. (2024)</i>										
HQP	1	19	94	122	-0.026	0.133	0.178	-0.003	0.122	0.206
	2	96	79	92	0.012	0.142	0.145	0.021	0.166	0.197
	3	25	80	94	-0.054	0.186	0.220	0.034	0.151	0.190
	4	12	84	95	-0.081	0.197	0.245	0.053	0.197	0.242
	5	13	93	112	-0.036	0.208	0.345	0.040	0.177	0.245
	6	17	97	111	-0.048	0.196	0.367	0.052	0.203	0.282
	7	40	95	109	-0.099	0.193	0.396	0.071	0.241	0.336
	8	162	164	167	-0.065	0.080	0.314	0.259	0.482	0.534
	9	56	144	183	-0.090	0.187	0.517	0.124	0.381	0.481
	10	21	110	132	-0.133	0.245	0.499	0.073	0.336	0.446
SCP	1	76	27	26	-0.007	0.008	0.008	-0.036	0.015	0.015
	2	95	83	106	0.012	0.149	0.156	0.010	0.181	0.224
	3	36	90	109	-0.058	0.197	0.229	0.051	0.185	0.257
	4	39	92	106	-0.131	0.195	0.253	0.137	0.277	0.346
	5	37	112	131	-0.122	0.232	0.331	0.138	0.304	0.405
	6	44	108	125	-0.187	0.218	0.322	0.194	0.372	0.471
	7	38	100	128	-0.196	0.277	0.444	0.170	0.360	0.478
	8	79	155	229	-0.096	0.193	0.487	0.255	0.500	0.575
	9	53	136	235	-0.136	0.249	0.620	0.243	0.467	0.562
	10	33	115	166	-0.305	0.430	0.568	0.231	0.478	0.579

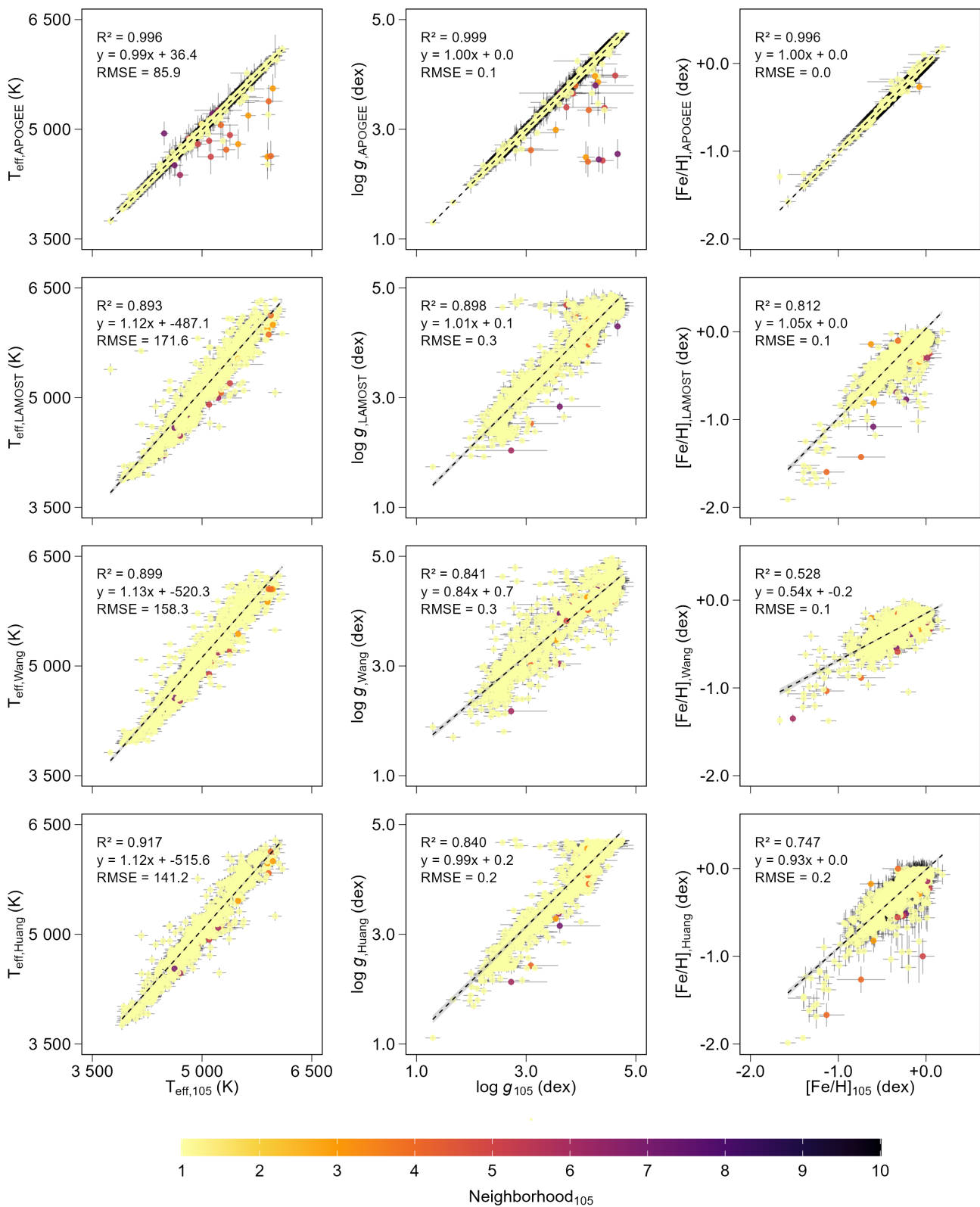


Fig. B.1. Comparison of the stellar parameter estimated by our method using 105 colors (x-axis) with those obtained from other sources (y-axis): LAMOST (first row), APOGEE (second row), Wang et al. (2022) (third row), and Huang et al. (2024) (fourth row). The color bar indicates the neighborhood index. The dashed line shows the best-fit linear regression, and the shaded region represents the 95% confidence interval of the fit. The regression equation, coefficient of determination (R^2) and the root mean square error (RMSE) are indicated in each panel. Each point includes the error values reported by the sources indicated on each axis.

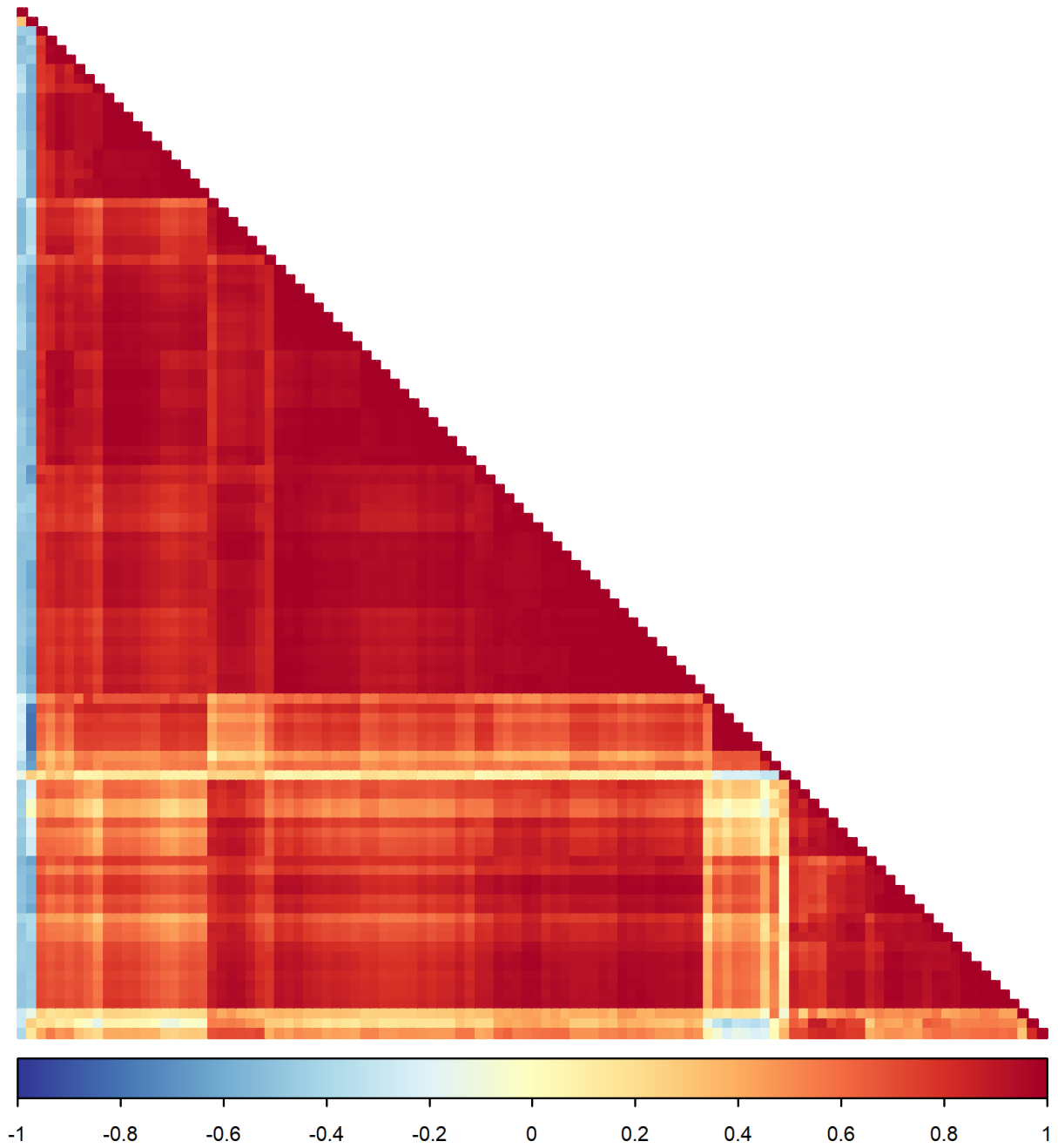


Fig. C.1. Matrix of correlation of parameters T_{eff} , $\log g$ and $[\text{Fe}/\text{H}]$, and the 105 colors obtained from the J-PLUS DR3 and 2MASS catalogs combined. Each row and column (105 in total) represent a color, order by their wavelengths, as indicated in Appendix C. The color bar indicates the different correlation values obtained.